Article

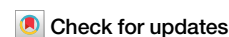# Tribocorrosion mechanism of biodegradable high-strength Zn-0.5Li alloy and pure Zn with bovine serum albumin adsorption

Check for updates

Bo-Yao Li[1], Wen-Bo Geng[1], Zhang-Zhi Shi[1,2] ✉, Wei Yin[1], Hai-Jun Zhang[3,4], Yu Yan[1], Da-Wei Zhang[1,5] & Lu-Ning Wang[1,2] ✉

High-strength biodegradable Zn alloys lack tribocorrosion studies. This study developed a Zn-0.5Li alloy achieving yield strength (307.5 MPa), ultimate tensile strength (466.5 MPa), and hardness (119.2 HV), 8.3, 4.7, and 3.6 times higher than pure Zn. In phosphate-buffered saline (PBS), the alloy's high strength and dense Li_3PO_4 corrosion products reduced wear by 70% compared to pure Zn. Under open-circuit potential conditions, material loss of the alloy comprises 12% mechanical wear, 85% corrosion-induced wear, and 3% wear-induced corrosion. Micro-galvanic corrosion between Zn and β-$LiZn_4$ phases promotes cracking and detachment, which enhances corrosion-induced wear. A 20 nm bovine serum albumin adsorption layer on the alloy surface forms after 24 h immersion, reducing wear area by 81% during tribocorrosion. This work establishes a microstructure-driven anti-tribocorrosion mechanism, guiding future Zn alloy design.

Tribocorrosion denotes the synergistic material degradation that occurs when a solid surface is simultaneously subjected to mechanical wear and/or electrochemical corrosion, leading to an accelerated material loss[1,2]. In the context of tribocorrosion, electrochemical reactions induced by corrosion can compromise the structural integrity of grain and phase boundaries, as well as other microstructural features[3]. This diminishes the binding strengths of these interfaces, rendering them more prone to spalling, consequently amplifying the extent of material wear[4,5]. Meanwhile, corrosive wear can thin or even destroy the passive film on the material's surface. It also increases the number of metal surface defects, including dislocations and vacancies[6–8]. Interactive effects of tribocorrosion can culminate in substantial material damage and expedite degradation of materials[9,10].

Metallic implants suffer corrosive wear in areas such as the oral cavity, joints, cardiovascular system, and gastrointestinal tract[11–15]. An artificial joint forms a frictional interface with bone, which is subjected to approximately 1–3 million cycles of corrosive wear annually[6,16–18]. This long-term corrosive wear can significantly shorten the service life of an artificial joint[19].

Moreover, corrosive wear can promote the release and migration of harmful metal ions from Ti alloys and stainless steels into the human body, posing health risks[20,21]. Material loss due to corrosive wear necessitates the frequent replacement of these implants. This not only increases economically burdensome on patients, but also subjects them to additional suffering due to the secondary surgery required for implant replacement[22,23]. Taking hip replacement as an example. Large-scale clinical data from the National Joint Registry reveal that among a total of 1.38 million hip replacements (2003–2017), approximately 10% were revision surgeries[19]. Of these, 12.5% of revisions were directly attributable to corrosive wear, equating to approximately 17,000 cases[19]. Notably, metal-on-metal prostheses exhibit significantly higher revision rates due to corrosive wear, primarily due to metal debris triggering adverse local tissue reactions and periprosthetic soft tissue necrosis.

Metallic implants can be categorized into non-degradable metals (e.g., Ti alloys[24], Co alloys[25], and stainless steels[26]) and degradable metals (e.g., Zn alloys[27], Mg alloys[28], and Fe alloys[29]). Research on corrosive wear mainly

[1]State Key Laboratory for Advanced Metals and Materials, Beijing Advanced Innovation Center for Materials Genome Engineering, School of Materials Science and Engineering, University of Science and Technology Beijing, Beijing, China. [2]Institute of Materials Intelligent Technology, Liaoning Academy of Materials, Shenyang, China. [3]Department of Interventional and Vascular Surgery, Shanghai Tenth People's Hospital, Tongji University School of Medicine, Shanghai, China. [4]National United Engineering Laboratory for Biomedical Material Modification, Branden Industrial Park, Qihe Economic & Development Zone, Dezhou City, Shandong, China. [5]Institute for Advanced Materials and Technology, University of Science and Technology Beijing, Beijing, China. ✉e-mail: ryansterne@163.com; luning.wang@ustb.edu.cn
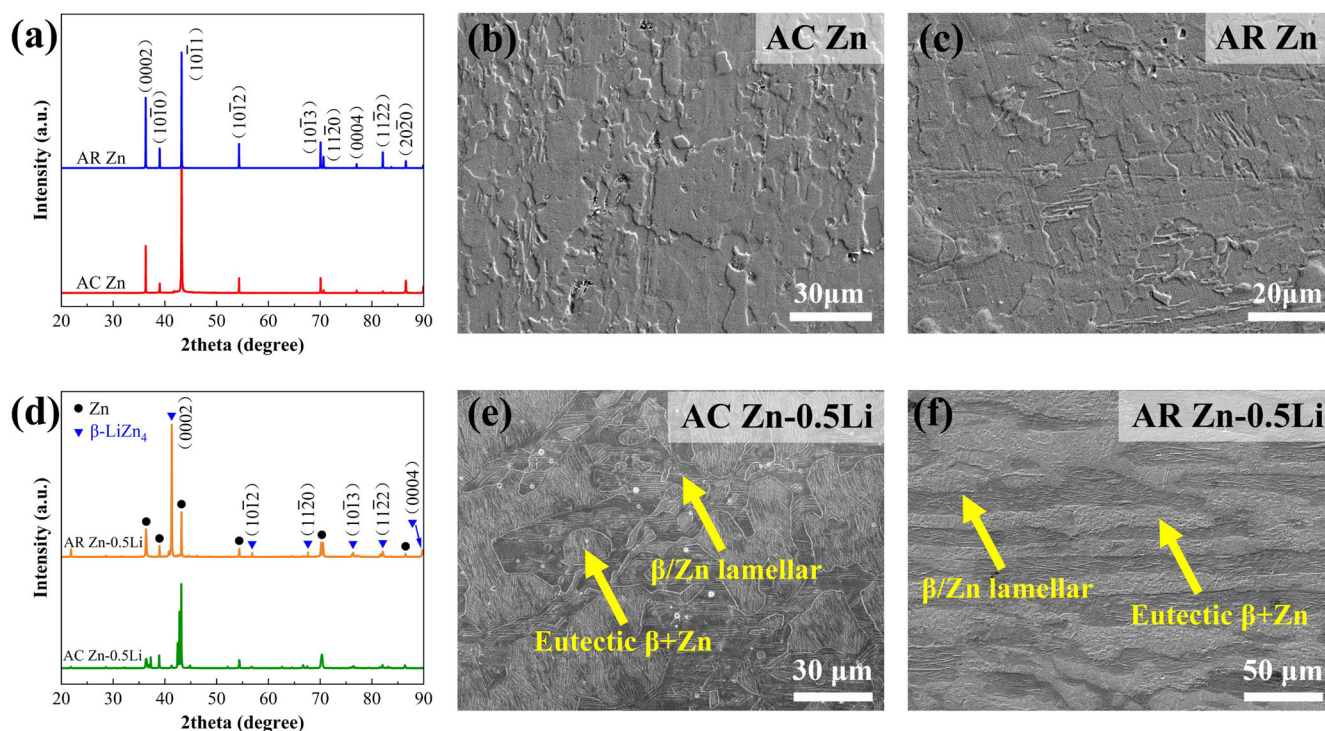
Fig. 1 | Phase composition and micro-morphology of pure Zn and Zn-0.5Li alloy. a XRD profiles of pure Zn; **b** Microstructure of the as-cast pure Zn; **c** Microstructure of the as-rolled pure Zn; **d** XRD profiles of Zn-0.5Li alloy; **e** Microstructure of the as-cast Zn-0.5Li alloy; **f** Microstructure of the as-rolled Zn-0.5Li alloy.

focus on non-degradable metals, with research on Zn alloys have just started[2,6,10,30]. Zn alloys exhibit a moderate degradation rate compared with Fe alloys and Mg alloys, possessing good biocompatibility and superior mechanical properties[31–34]. As an essential trace element for the human body, the osteogenic properties of Zn make Zn alloys promising for applications in orthopedic implants[35–39]. Nontoxic elements such as lithium (Li) have been selected as alloying elements in biodegradable Zn alloys. The addition of Li can significantly enhance yield strengths (YSs) and ultimate tensile strengths (UTSs) of Zn alloys[40]. Zn-Li alloys have demonstrated comparable strength to those of commercially used pure titanium and stainless steels. Additionally, Zn-Li alloys have a beneficial impact on new bone formation, indicating their potential for use in high-load-bearing orthopedic implants[41,42]. The Zn-0.5Li alloy developed in this study exhibits a YS of 307 MPa, a UTS of 466 MPa, and an EL of 52.3%, meeting the strength requirements for rib fixation plates (YS > 230 MPa, UTS > 300 MPa, EL > 15%[43]). Additionally, the alloy demonstrates outstanding antibacterial properties and excellent biocompatibility, demonstrating significant promise for rib fixation plate applications[43]. For Zn-Li alloys, tribocorrosion may lead to excessive release of Zn^{2+}, which can inhibit the activity of osteoblasts. The debris generated from wear may also cause local inflammation[43]. The ideal degradation rate should match the rate of new bone growth. If tribocorrosion leads to premature failure, the implant will fail to provide stable mechanical support, which may result in delayed bone healing or deformity. As an internal fixation device for fractures, rib plates are subject to continuous friction between the screws and plate holes, and between the bone plate and bone surface due to breathing and muscle movement[43]. Therefore, their tribocorrosion resistance should be considered. Body fluid environment contains not only inorganic components such as Na^+, Ca^{2+}, Cl^-, HCO_3^-, and HPO_4^{2-} ions, but also organic compounds like amino acids, glucose, and proteins. Albumin, the most abundant plasma protein (~60% of total protein content), dictates protein adsorption at implant surfaces and, consequently, exerts a pronounced influence on their tribocorrosion. Bovine serum albumin (BSA) is adopted as a standard model protein in tribocorrosion studies of biomedical alloys

due to its structural similarity to human serum albumin. Previous studies have found that BSA can significantly reduce the tribocorrosion of Zn-Mn alloy[44]. However, there is currently a lack of research on the effect of BSA on tribocorrosion behaviors of Zn-Li alloys. In this work, the interaction effects of corrosion and wear for biodegradable Zn-0.5Li alloy and the influence of BSA during tribocorrosion in phosphate-buffered saline (PBS) are investigated.

Results

Microstructure

X-ray diffraction (XRD) patterns of as-cast (AC) and as-rolled (AR) Zn and Zn-0.5Li alloy are presented in Fig. 1a, d. Compared to Zn (AC), the diffraction peak intensity of Zn (AR) at (0002) is significantly increased, indicating a change in crystal orientation during the rolling process. Figure 1d shows that both Zn-0.5Li (AC) and Zn-0.5Li (AR) alloys are mainly composed of Zn and β-$LiZn_4$ phases. In the AR state, the β-phase diffraction peaks exhibit a significant enhancement in intensity at (0002), indicating a basal texture typical for rolled HCP metals[45].

Figure 1b, c shows the scanning electron microscope (SEM) microstructure of Zn (AC) and Zn (AR). Figure 1e shows the SEM microstructure of Zn-0.5Li (AC) alloy, which consists of primary β-$LiZn_4$ in a dendrite-like shape or an elliptical shape and eutectic Zn and β-$LiZn_4$. There is supersaturated precipitation of fine white Zn filaments in β-$LiZn_4$, which form a laminated structure of β-$LiZn_4$/Zn. The remaining part is the eutectic structure of Zn + β-$LiZn_4$, with the lighter-contrast Zn phase and the darker-contrast β-$LiZn_4$ phase alternating. After rolling, the original as-cast structure deforms into a fibrous shape along the rolling direction under compressive stress, as shown in Fig. 1f. Li has a negative standard electrode potential of −3.04 V, much lower than that of Zn (i.e., −0.76 V), so that β-$LiZn_4$ is more vulnerable to the attack of the etching solution. No matter whether β-$LiZn_4$ is in the primary β-$LiZn_4$ or in the eutectic, it is always corroded more quickly than its surrounding Zn, resulting in a recessed topography and a darker color[45].

Mechanical properties

The engineering tensile stress-strain curves of Zn (AR) and Zn-0.5Li (AR) alloy are shown in Fig. 2. Curves of Zn (AC) and Zn-0.5Li (AC) alloy are not depicted in Fig. 2 due to their low ELs (1.7% and 0.5%, respectively). Tensile mechanical properties and hardness of Zn and Zn-0.5Li alloy are listed in Table 1. The Zn-0.5Li (AC) alloy exhibits YS, UTS, and EL of 185.4 MPa, 197.3 MPa, and 0.5%, respectively. The rolling process eliminates the brittleness and greatly elevates the EL to 52.3% (i.e., 104.6 times increase). Concurrently, the rolling process enhances the strength of the alloy,
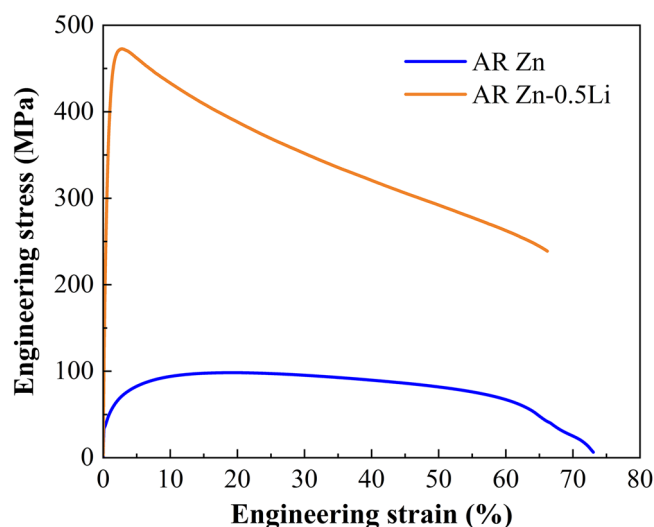

Fig. 2 | Mechanical properties of pure Zn and Zn-0.5Li alloy. Engineering strain-stress curves of Zn (AR) and Zn-0.5Li (AR) alloy.

Table 1 | Tensile properties and hardness of Zn and Zn-0.5Li alloy

Materials	Tensile properties			Hardness
	YS/MPa	UTS/MPa	EL%	HV
AC Zn	36.8 ± 2.4	38.4 ± 1.9	1.7 ± 0.23	32.3 ± 3.1
AR Zn	37.4 ± 1.9	99.4 ± 5.6	66.5 ± 7.1	33.2 ± 2.4
AC Zn-0.5Li	185.4 ± 9.2	197.3 ± 6.9	0.5 ± 0.1	117.8 ± 4.6
AR Zn-0.5Li	307.5 ± 1.9	466.5 ± 9.2	52.3 ± 1.7	119.2 ± 4.1

significantly elevating the YS to 307.5 MPa (i.e., 65.9% increase) and the UTS to 466.5 MPa (i.e.,136.4% increase), respectively.

Hardness of Zn-0.5Li (AR) is 119.2 HV, which is about 3.6 times that of Zn (AR). The rolling process has a negligible effect on the hardness of both materials. Alloy element Li enhances the strength and hardness of pure Zn without compromising its plasticity. This is attributed to the β-LiZn$_4$/Zn lamellar structure in Zn-0.5Li alloy, which possesses both high strength and high ductility[46].

Corrosion and wear results

Under the premise of rough contact surfaces and elastic conditions, the wear model proposed by Archard shows[47]:

$$\Delta V = K \frac{NL}{H}, \tag{1}$$

where ΔV (10^{-3} mm^3) is the wear volume, N (N) is the applied load, L (mm) is the sliding distance, H (HV) is the material's hardness, and K is a wear coefficient. Figure 3a shows the coefficient of friction (COF) curves of pure Zn and Zn-0.5Li alloys immersed in the PBS for 1 h under open-circuit potential (OCP) conditions. Following 30 s of corrosive-wear testing, COF curves of all the specimens reach a stable state. The COF of pure Zn exhibits greater fluctuation, a phenomenon attributed to its lower hardness, resulting in more pronounced fluctuations in the axial load throughout the frictional process. The average COF for Zn-0.5Li alloy is 0.52, which is 63% of that of the pure Zn (Fig. 3b).

Hardness of Zn-0.5Li alloy is about 3.6 times that of pure Zn (Table 1). Based on Eq. (1), it can be inferred that the volume change for Zn-0.5Li alloy should be only 28% of that of the pure Zn, which is consistent with the experimental results (Fig. 3b).

Surface morphologies of the samples after tribocorrosion tests are shown in Fig. 4. The rolling direction is designated as RD. Pure Zn samples exhibit larger scratches with a smooth base at the bottom. On both sides of the scratches, there are ridge-like metal accumulations 5–9 μm higher than the base surface, indicating significant plastic deformation. In contrast, Zn-0.5Li alloy samples exhibit no metal accumulations on the surface, while the bottom of the scratches features micro-furrows parallel to the sliding direction. The plastic deformation of pure Zn led to the extrusion and accumulation of material on either side of the scratch, thereby maintaining the overall mass despite the substantial volume change (Fig. 3b). Figure 4e shows the cross-sectional morphologies of the scratches. The scratch of Zn (AC), with a width of 1.06 mm and a depth of 19.99 μm, has the largest corresponding volume change at 0.17 mm^3. The scratch width and depth of the alloy samples are both significantly smaller than those of the pure Zn
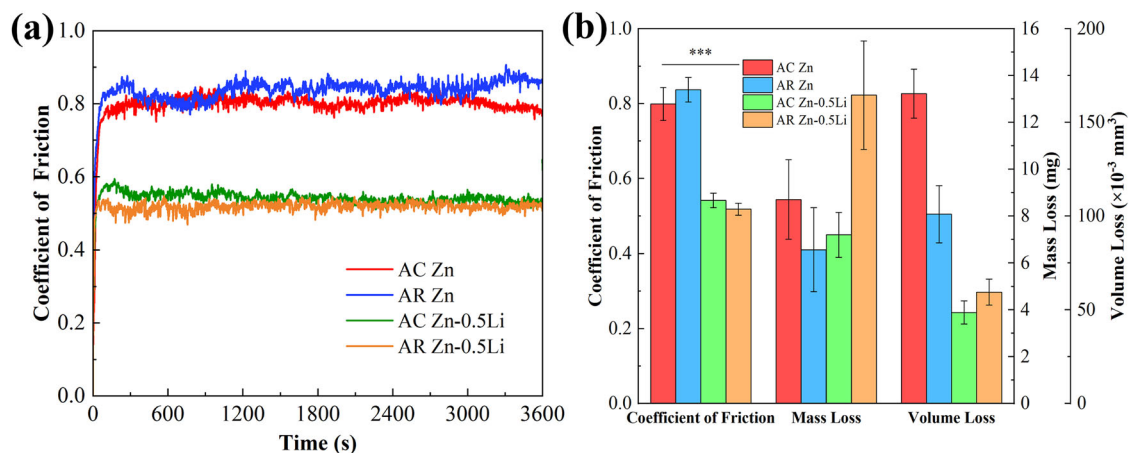

Fig. 3 | Wear resistance of pure Zn and Zn-0.5Li alloy. Pure Zn and Zn-0.5Li alloy subjected to corrosion wear in PBS solution for 1 h: **a** COF curve; **b** Bar chart of COF, mass loss, and volume change.
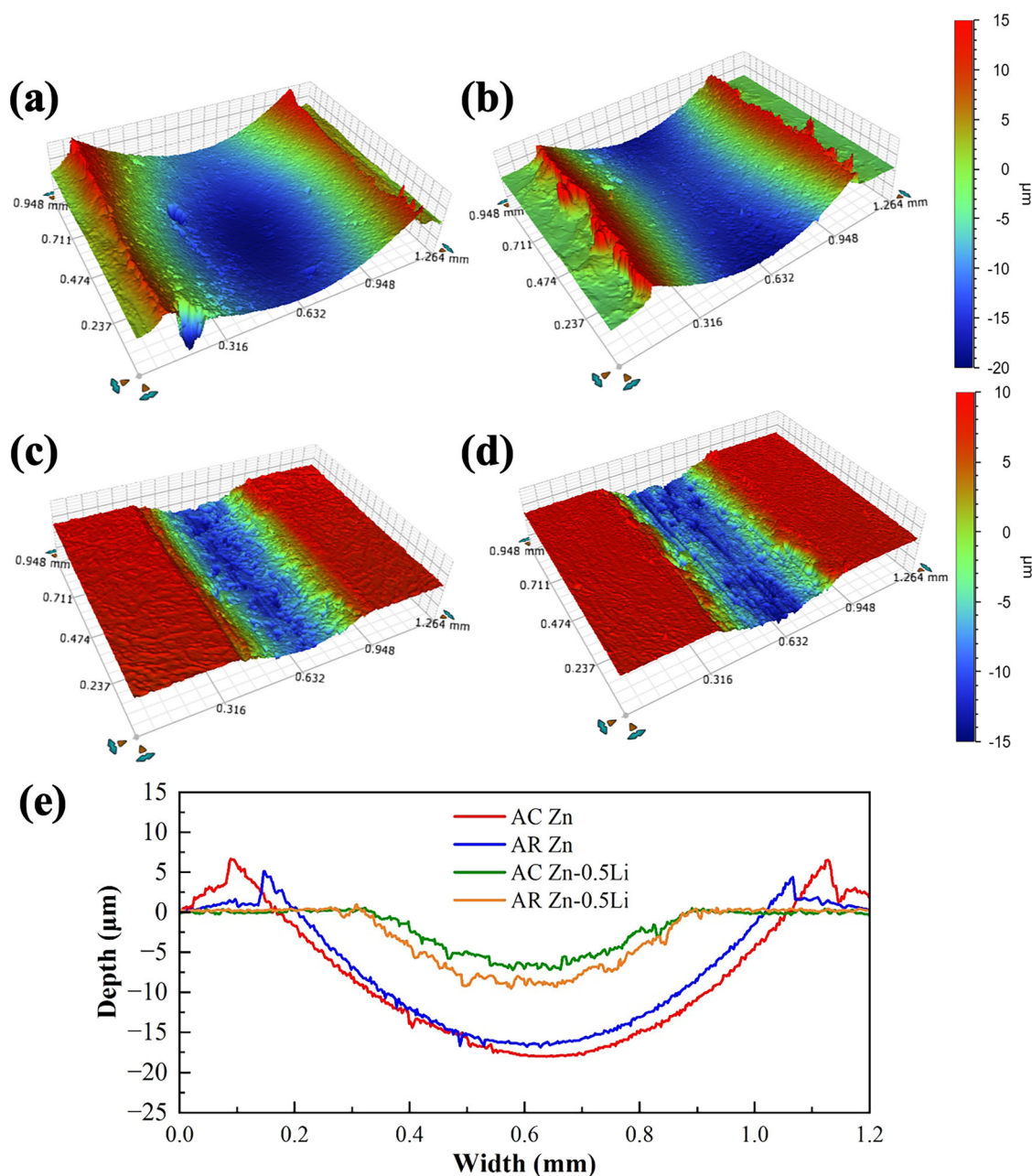
Fig. 4 | Scratch morphology of pure Zn and Zn-0.5Li alloy after tribocorrosion. a Zn (AC); **b** Zn (AR); **c** Zn-0.5Li (AC); **d** Zn-0.5Li (AR); **e** cross-sectional morphologies of the scratches.

samples. Pure Zn (AR) and Zn-0.5Li (AR) have a roughness of 5.89 ± 1.55 μm and 2.71 ± 0.42 μm, respectively.

SEM images of the surface morphology of pure Zn and Zn-0.5Li alloy after corrosion wear are presented in Figs. 5 and 7, respectively. Pure Zn samples exhibit wider scratches. The substrates adjacent to the scratches on both sides exhibit varying degrees of extrusion deformation. Zn (AC) exhibits a wrinkled appearance (Fig. 5a), while Zn (AR) exhibits a flaky appearance (Fig. 5d). Some substrate materials and friction products are extruded and accumulated along the sides of the scratches of Zn (AR), forming plastic buildups. Compared to pure Zn, the scratches on Zn-0.5Li alloy samples are narrower. No plastic buildup along scratches is observed on both the Zn-0.5Li (AC) and Zn-0.5Li (AR) alloys, and adhesive wear is present on their surfaces (Figs. 6a and 7d). The adhesive wear areas in Zn-0.5Li (AC) alloy are mainly concentrated at the edges of the scratches (Fig. 6a), while in Zn-0.5Li (AR) alloy, they are larger and irregularly distributed over the scratch surface (Fig. 6d).

Pure Zn samples experience fatigue wear. Cracks and spalling pits are distinctly observable on the scratch surface of Zn (AC) (Fig. 5c), while a sparse number of fine fatigue cracks are observed on Zn (AR) (Fig. 5f). As for Zn-0.5Li alloy samples, scratch surfaces show a groove shape along with the friction direction, which are typical abrasive wear morphologies (Fig. 6c, f). The appearance of the abrasive wear effect is due to the fall off of micro-asperities between the two contact surfaces to form abrasive chips, which will produce microscopic grooves on the surface[48]. Additionally, there are local areas where material is detached, forming spalling pits (Fig. 6c). Therefore, Zn-0.5Li alloy samples experience a mixed wear mechanism of adhesive, abrasive, and fatigue wear.

EDS elemental mapping results for pure Zn samples show that P and O are enriched in the scratches after the corrosion wear process, while C is uniformly distributed (Figs. 5b and 6e). However, no accumulation of P and O is observed in the scratches on Zn-0.5Li alloy samples (Figs. 6b and 7e).
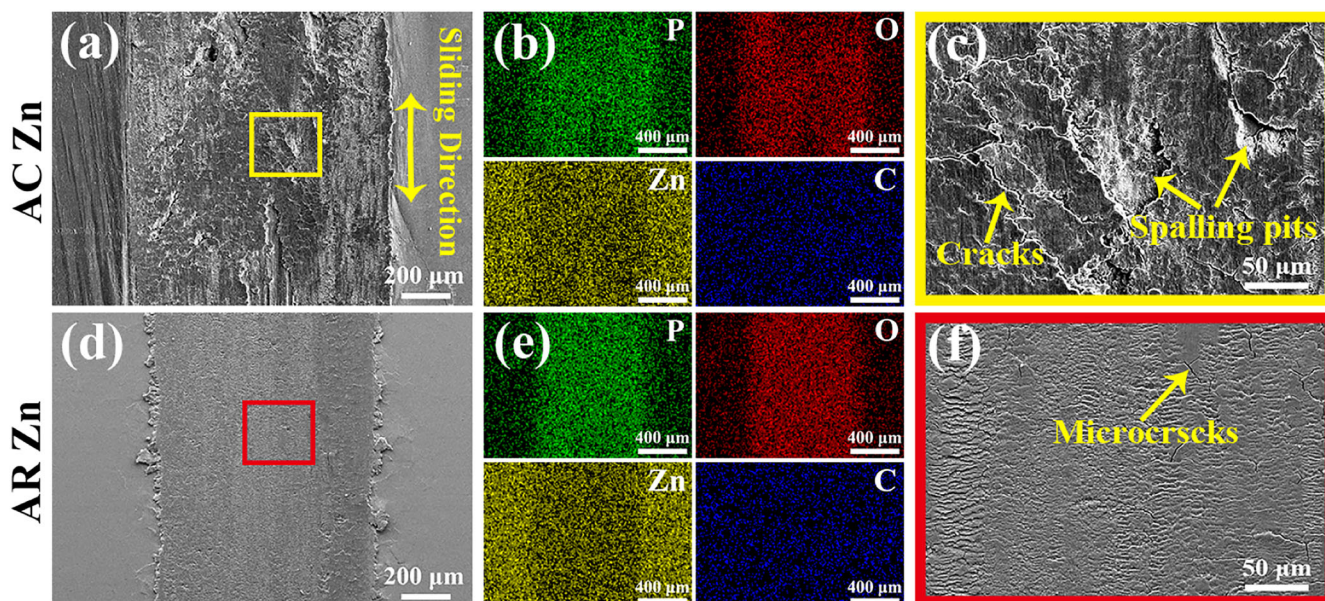
Fig. 5 | Micro-morphology and elemental distribution of the scratches on pure Zn after 1 h tribocorrosion. a, **c** SEM images of Zn (AC); **b** EDS images of Zn (AC); **d**, **f** SEM images of Zn (AR); **e** EDS images of Zn (AR).
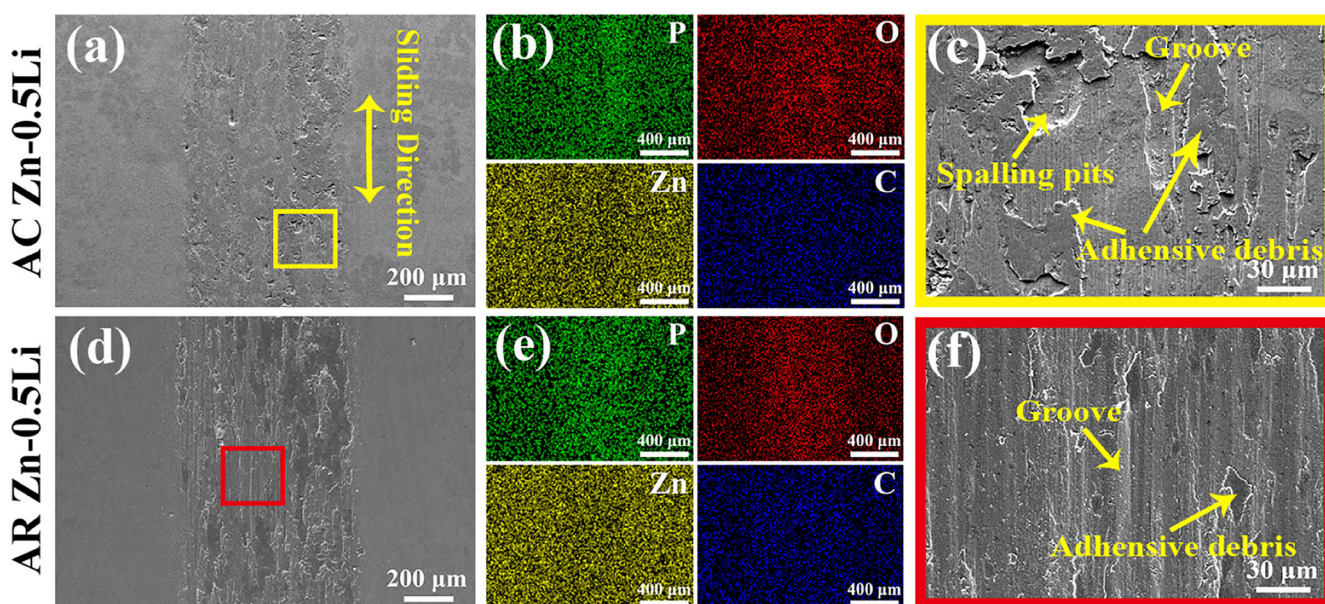

Fig. 6 | Micro-morphology and elemental distribution of the scratches on Zn-0.5Li alloy after 1 h tribocorrosion. a, **c** SEM image of Zn-0.5Li (AC); **b** EDS images of Zn-0.5Li (AC); **d**, **f** SEM image of Zn-0.5Li (AR); **e** EDS images of Zn-0.5Li (AR).

The X-ray photoelectron spectrometer (XPS) results of the scratch surfaces of pure Zn and Zn-0.5Li alloy are shown in Fig. 7. The corrosion products on the surface of pure Zn are mainly ZnO, $ZnCO_3$, and $Zn_3(PO_4)_2$. In addition to these three corrosion products, the surface of the Zn-0.5Li alloy also contains Li_3PO_4. A more detailed discussion will be presented in the section "Discussion."

The presence of wear debris significantly influences the corrosive wear system. Wear debris typically manifests as irregularly shaped particles, which are primarily generated through two mechanisms: (1) The adhesion and delamination process that yields flaky or chunky metallic debris; (2) During frictional pairs sliding, severe shear deformation caused by hard abrasive particles leads to the formation of ribbon-like metallic debris[49]. Pure Zn debris is

characterized as blocky and flaky particles, with dimensions typically ranging from 20 to 50 µm (Figs. 8a and 9c). Zn-0.5Li alloy debris is predominantly thin and flaky, spanning from 50 to 100 µm (Fig. 8b, d). Pure Zn corresponds to mechanism (1), while Zn-0.5Li alloy corresponds to mechanism (2).

Wear debris from Zn (AC) and Zn-0.5Li (AC) alloy exhibits a layered structure on their surfaces and edges (red dashed areas in Figs. 8a and 9b). This is due to the generation and propagation of fatigue cracks. Under the influence of reciprocating friction, dislocations accumulate near the subsurface of the scratch, leading to stress concentration and the nucleation of cracks[50]. These cracks continue to propagate, extending upwards to the surface of the scratch and fracturing to form flaky wear debris, as shown in Figs. 8a and 9b.
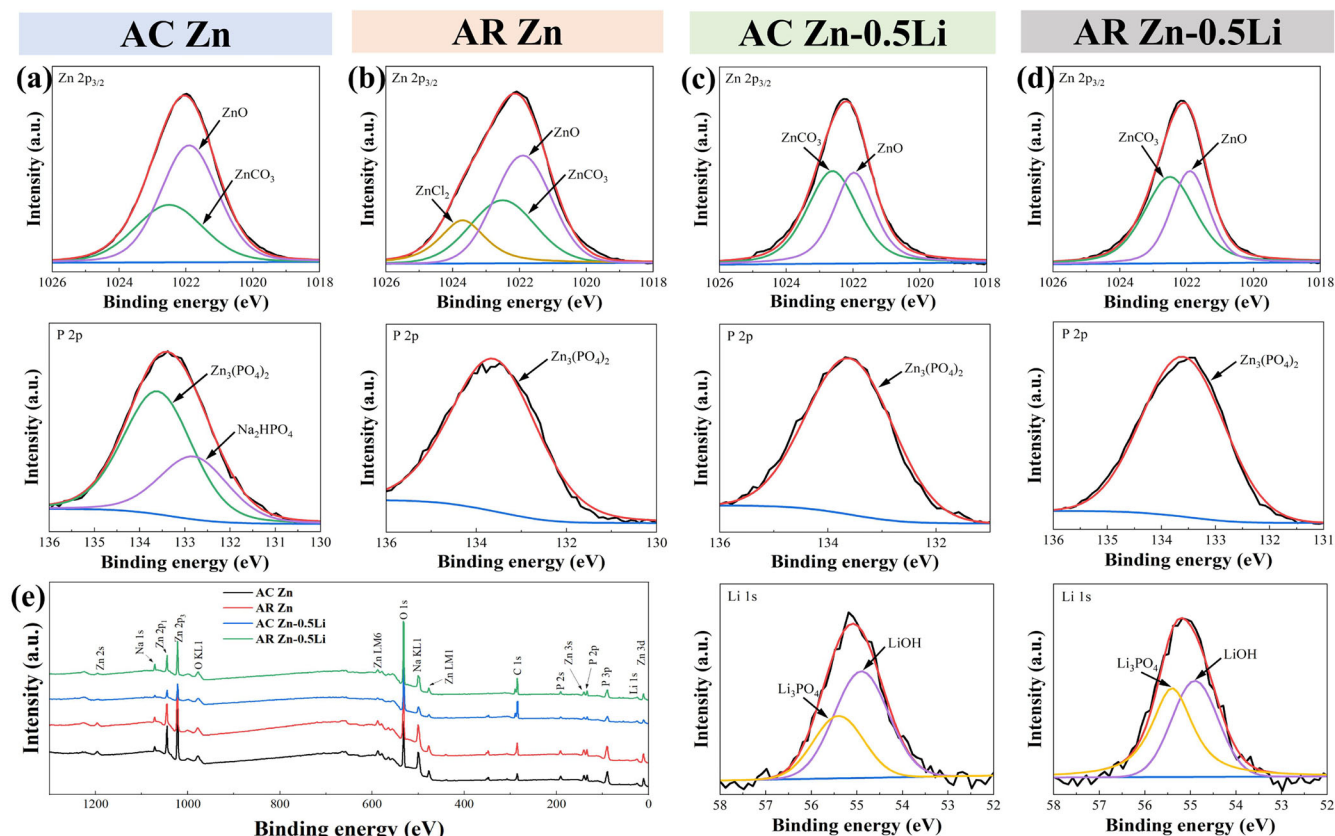
Fig. 7 | Types of corrosion products on the scratches of Zn-0.5Li alloy after 1 h tribocorrosion. High-resolution XPS spectra of the worn surface of samples after 1 h tribocorrosion in PBS solution: **a** AC Zn; **b** AR Zn; **c** AC Zn-0.5Li; **d** AR Zn-0.5Li; **e** Full-spectra XPS.
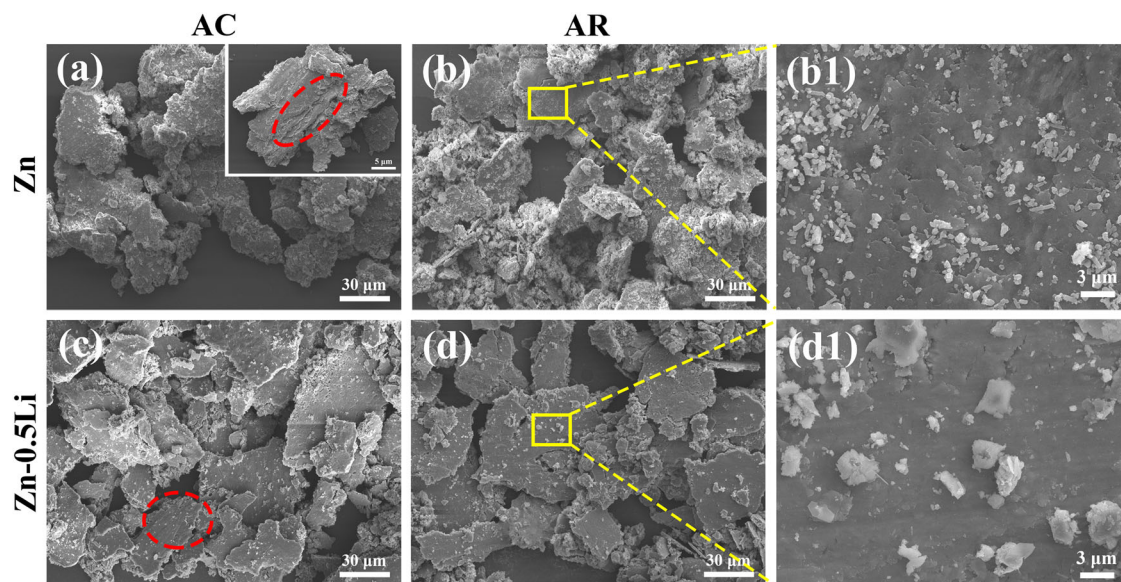

Fig. 8 | Wear debris morphology of pure Zn and Zn-0.5Li alloy after tribocorrosion. a, c are wear debris of Zn (AC) and Zn (AR), **c1** is a magnification of (**c**); **b, d** are wear debris of Zn-0.5Li (AC) and Zn-0.5Li (AR), **d1** is a magnification of **d**.

Figure 8c1, d1 shows the magnification of the corroded areas on the wear debris surfaces of Zn (AR) and Zn-0.5Li (AR) alloy. Debris of Zn (AR) is severely corroded, with a significant amount of rod-shaped, spherical, and blocky corrosion products. Smaller debris particles aare lmost entirely covered by these corrosion products. Debris of Zn-0.5Li (AR) alloy shows the formation of lumped corrosion products, with the corrosion being less severe than that observed in Zn (AR).

Interaction of corrosion and wear

For practical engineering applications, as-rolled Zn alloy can be used to manufacture biodegradable bone plates and other products[45]. Figure 9a

shows the polarization curves of Zn (AR) and Zn-0.5Li (AR) in the PBS at room temperature, whose parameters are obtained by Tafel extrapolation (as shown in Table 2). E_{corr} and i_{corr} of Zn (AR) are -1.12 V and $0.24\,\mu\text{A cm}^{-2}$, and that of Zn-0.5Li (AR) are -1.10 V and $0.22\,\mu\text{A cm}^{-2}$, respectively. In subsequent corrosion wear potentiostatic experiments, the cathodic protection potential was set to -1.3 V, the anodic corrosion potential was set to -0.9 V, and a potential of -1.1 V was set to simulate the self-corrosion state (OCP) of the samples.

Electrochemical impedance spectroscopy (EIS) measurements are shown in Figs. 9b and 10c. Generally, the time constant of the electrochemical process is indicated by the peak of the -phase angle vs. frequency curves in the Bode plot. The number of peaks corresponds to the number of components in the circuit[44]. The -phase angle vs. frequency curves of the alloy wire exhibit two distinct peaks (Fig. 9b). Accordingly, a double time constant equivalent circuit is employed to fit the EIS results (Fig. 9c). The parameters of the components in the circuit diagram are shown in Table 3. R_s is the solution resistance. R_{ct} is the charge transfer resistance between the sample and PBS solution. R_c is the resistance of the corrosion product layer. C_c is the capacitance of the corrosion product layer. Q_{dl} is the constant phase angle element. Y_0 is the admittance form of the constant phase angle element. n is the exponent in the constant phase angle element. In the simulation circuit, the Warburg diffusion element "W" exhibits a 45° line in the low-frequency range. In the high-frequency region, the capacitive loop diameter of Zn-0.5Li (AR) is larger than that of Zn (AR). This indicates that the alloy exhibits a higher Rct (in Table 3), which means that the charge transfer step in the corrosion reaction is more significantly hindered[44]. In the low-frequency region, the larger capacitive loop diameter of the alloy similarly demonstrates more prominent diffusion resistance[44]. Therefore, the alloy possesses superior corrosion resistance. Values of R_{ct} and R_c of Zn-

Table 2 | Electrochemical parameters of the alloys

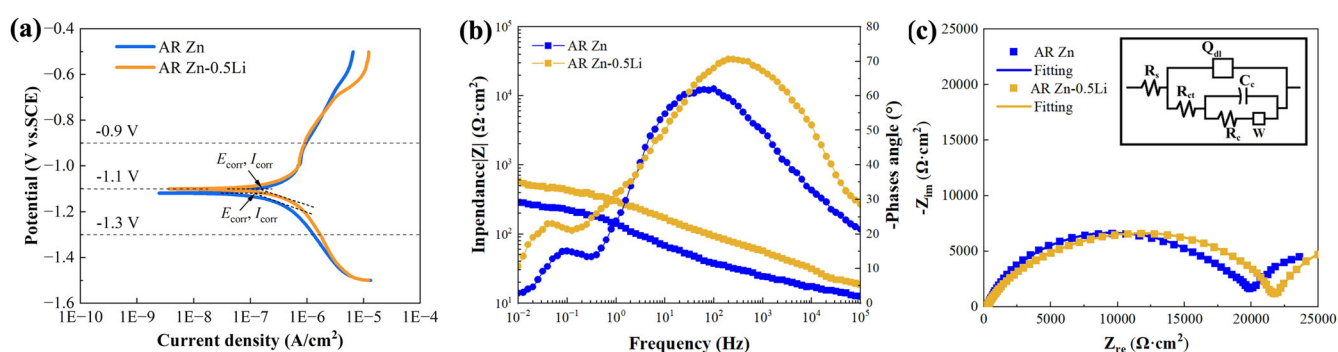| Alloy	E_{corr} (V)	I_{corr} (μA/cm^2)
AR Zn	-1.12 ± 0.08	0.24 ± 0.04
AR Zn-0.5Li	-1.10 ± 0.02	0.22 ± 0.01

Fig. 9 | Electrochemical properties of Zn (AR) and Zn-0.5Li (AR) alloy in PBS. a Polarization curve; **b** Bode plots; **c** Nyquist and equivalent circuit plots.

Fig. 10 | Time-dependent open-circuit potential and current evolution of Zn (AR) and Zn-0.5Li (AR) during tribocorrosion. a OCP curves of Zn (AR) and Zn-0.5Li (AR) alloy; Current-time curves during corrosion wear at potentials of: **b** -1.3 V; **c** -1.1 V; **d** -0.9 V.
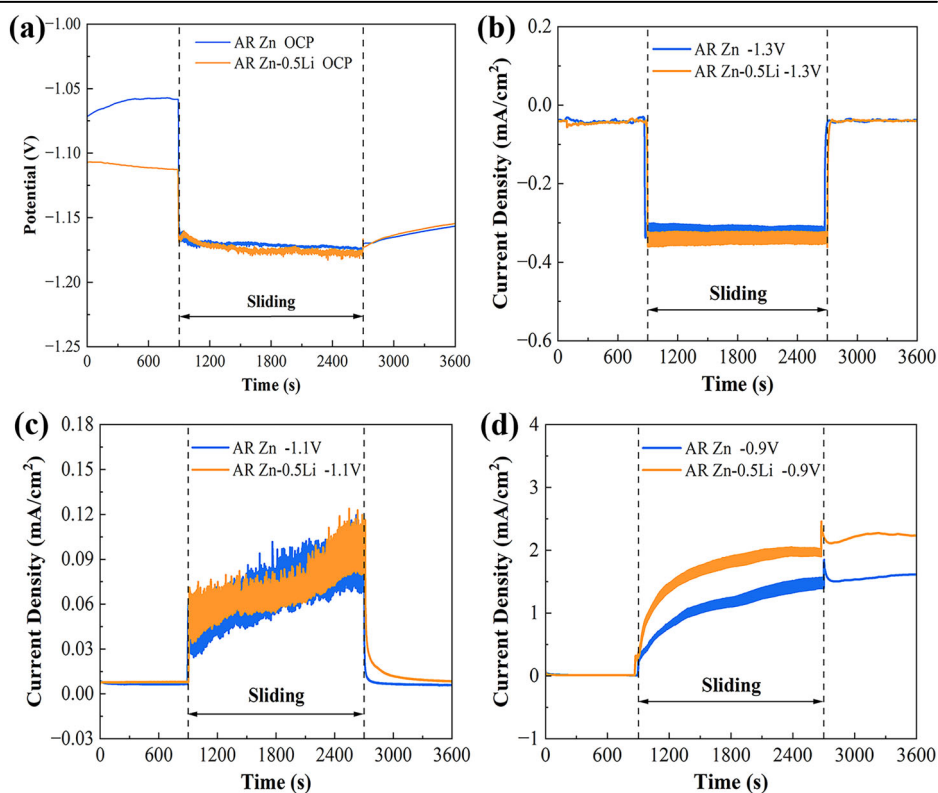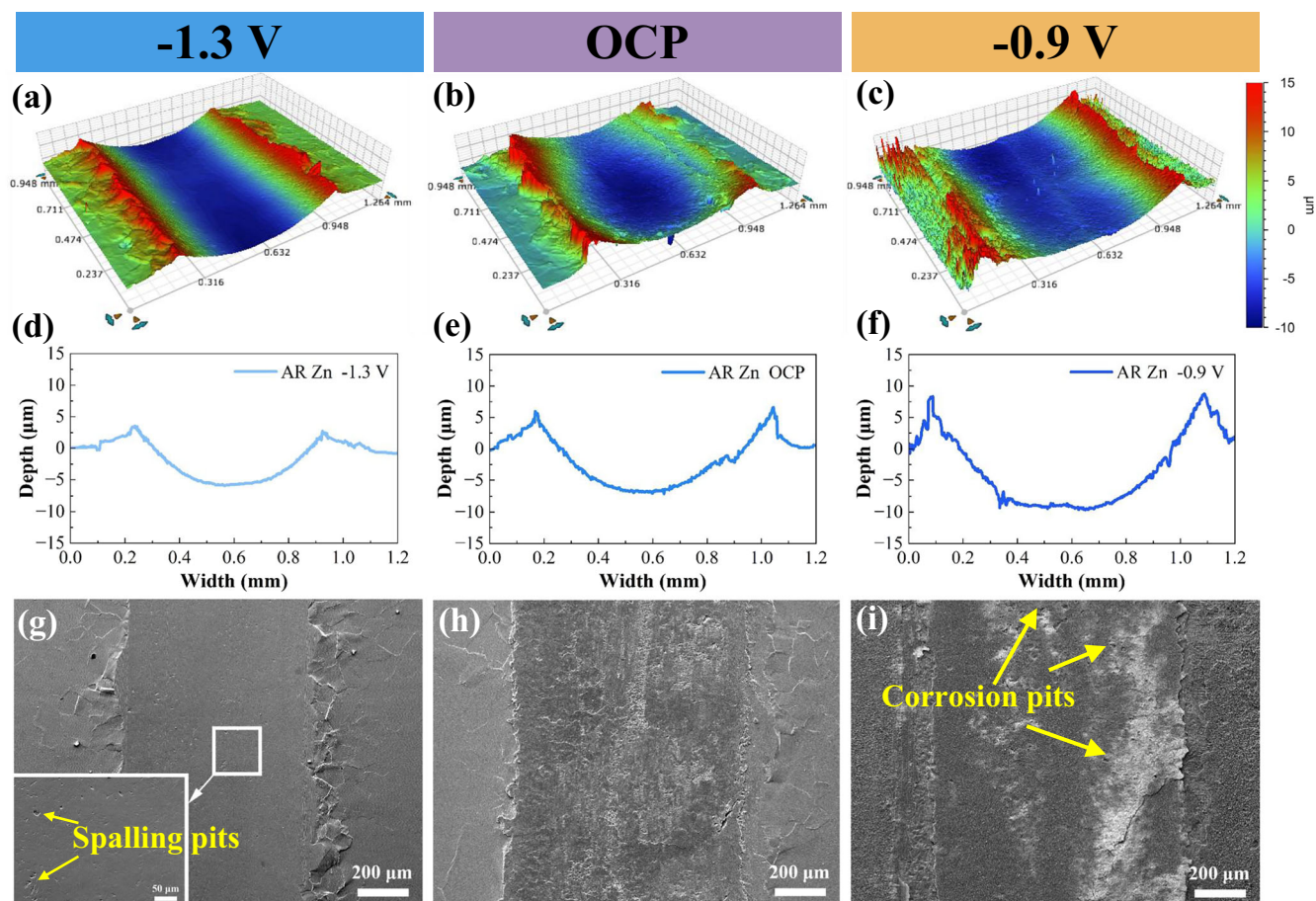
Table 3 | Impedance spectroscopy (EIS) fitting data of Zn (AR) and Zn-0.5Li (AR) alloy

Alloy	R_s (Ω cm^2)	Q_{dl}		R_{ct} (Ω cm^2)	C_c (10^{-6}F/cm^2)	R_c (Ω cm^2)	$W \times 10^{-4}$ (Ω cm^2 S$^{-0.5}$)
		$Y_0 \times 10^{-6}$ (Ω^{-1}cm^{-2}S^{-n})	n				
AR Zn	215.3 ± 0.90	0.96 ± 0.03	0.77 ± 0.46	1799 ± 15.59	0.25 ± 0.09	1625 ± 2.81	63.2 ± 1.1
AR Zn-0.5Li	221.0 ± 0.64	1.62 ± 0.02	0.72 ± 0.39	2210 ± 3.31	2.83 ± 0.04	3196 ± 22.66	43.5 ± 5.2

Fig. 11 | Wear scratch morphology of Zn (AR) at different potentials. a–c Three-dimensional morphologies, **d–f** cross-sectional profiles, **g–i** micro-morphologies.

0.5Li (AR) are larger than those of Zn (AR) (as shown in Table 3), also indicating a better corrosion resistance of Zn-0.5Li (AR).

Fig. 10a shows the variation of the OCP over time for Zn (AR) and Zn-0.5Li (AR) alloy in the PBS. Initially (i.e., about 900 s), the potential values are comparatively high, signifying the integrity of passive films on the surfaces of both the metal. This phenomenon also occurs in Zn-0.4Mn alloy[44]. After 900 s, when corrosion wear begins, the potentials of all the samples decrease to form a lower platform due to the destruction of the passivation layer. At the end of the tribocorrosion test, potentials gradually increase.

Figure 10b–d shows curves of the current density as time progresses for Zn (AR) and Zn-0.5Li (AR) alloy under various potentiostatic conditions. As shown in Fig. 10b, both samples exhibit negative current density under the application of −1.3 V cathodic protection potential. Prior to the initiation of corrosive wear, the current density decreases from −0.04 mA/cm² to −0.33 mA/cm². Once the test ceases, it reverts to its initial value. Cathodic protection controls the corrosion component in the total material loss. The sample loss is entirely attributable to mechanical wear.

As shown in Fig. 10c, when the applied potential (−1.1 V) is near the self-corrosion potential, the current density for both samples is positive. After the initiation of corrosion wear, it shows an upward trend, indicating the occurrence of electrochemical corrosion. Once the test ceases, the

current density drops rapidly back to the pre-friction level. As shown in Fig. 10d, −0.9 V anodic corrosion potential is applied. After the initiation of corrosion wear, current densities of both samples persistently rise. At the end of the tribocorrosion test, the current density is 1.5 mA/cm² for Zn (AR), and 1.9 mA/cm² for Zn-0.5Li (AR) alloy. Following the termination of corrosion wear, the current density shows a tendency to persist in rising. During corrosion wear tests at −1.1 V and −0.9 V, the sample loss includes material loss due to corrosion, mechanical wear, and the interactive effects of the former two.

Figures 11 and 12 show scratch morphologies and cross-sectional profiles of Zn (AR) and Zn-0.5Li (AR) alloy after 30 min of corrosive wear with the applied potential of −0.9 V, −1.1 V (OCP), and −1.3 V. At −1.3 V, plastic deformation is evident along the sides of the scratch of Zn (AR) (Figs. 11a and 12g), measuring 0.69 mm in width and 5.89 μm in depth (Fig. 11d). The scratch surface appears smooth, with observable small spalling pits and an absence of fatigue cracks (Fig. 11g). As for Zn-0.5Li (AR) alloy, the width and depth of the scratch are only 0.3 mm and 0.13 μm (Fig. 12d), with the scratch surface exhibiting some minor grooves (Fig. 12a, g).

At −1.1 V (OCP), an increased number of fatigue cracks are exhibited on the scratch surface of Zn (AR) (Fig. 11h), with a corresponding enlargement in width and depth compared to −1.3 V condition (Figs. 11b and 12e). As for Zn-0.5Li (AR), the scratch expands (Figs. 12b and 13e),
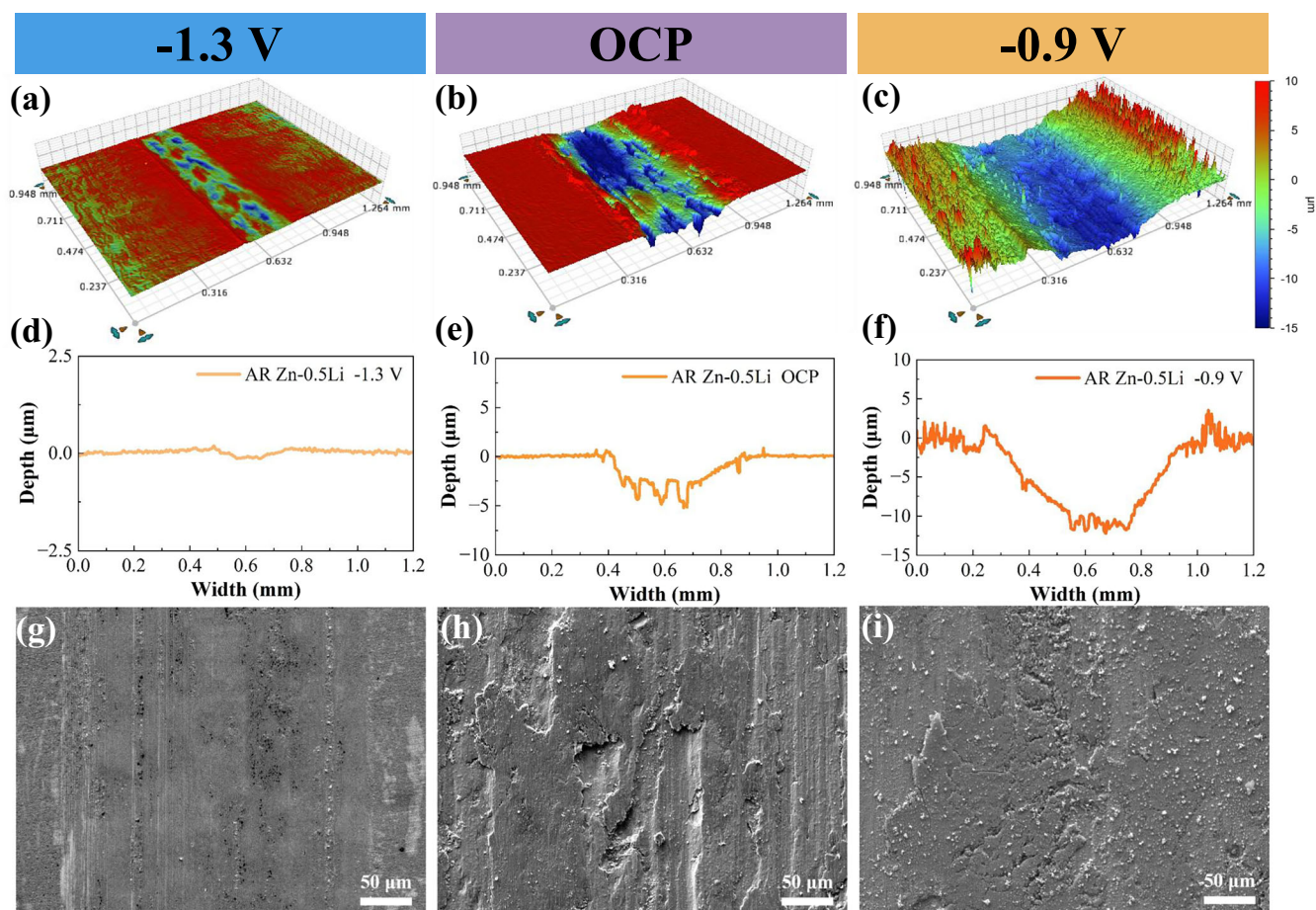
Fig. 12 | Wear scratch morphology of Zn-0.5Li (AR) at different potentials. a–c Three-dimensional morphologies, **d–f** cross-sectional profiles, **g–i** micro-morphologies.

lamellar exfoliation appears on the surface, and the edges of the scratch are rough and irregular (Fig. 12h).

At −0.9 V, as for Zn (AR), the electrochemical action intensifies corrosion, resulting in a layer of corrosion products covering the material surface (Fig. 11i). Corrosion pits are distributed over the scratch surface, leading to further material loss. The scratch widens to 0.99 mm and deepens to 9.61 μm, with significant fatigue cracks and extensive material spalling on both sides of the scratch (Figs. 11c and 12f, i). As for Zn-0.5Li (AR), a significant amount of white, fluffy corrosion products formed on both the scratch and the adjacent substrate, indicating intensified corrosion wear (Fig. 12c, f, i).

Influence of BSA on tribocorrosion

Pure Zn (AR) and Zn-0.5Li (AR) alloys are immersed in PBS solution with 10 g/L BSA for 24 h. Subsequently, surface morphologies are observed using a fluorescence microscope, and the thickness of the BSA adsorption layers is analyzed by XPS (Fig. 13). As shown in Fig. 13a1, a2, after 24 h immersion, the sample surfaces are covered by BSA, which shows green color. XPS is employed for elemental depth profiling, with each sputtering cycle removing 5 nm of material, repeated for a total of 10 cycles. As shown in Fig. 14b1, after sputtering to a depth of 10 nm on the pure Zn (AR) surface, the content of O, N, and P elements approaches zero, while the content of C and Zn elements stabilizes without further fluctuation. Based on these observations, we infer that the thickness of the BSA adsorption layer is 10 nm. For the corresponding Zn-0.5Li (AR) alloy, the thickness of the BSA layer is 20 nm (Fig. 13b2).

Additionally, high-resolution XPS spectra of C 1s and N 1s on Zn (AR) and Zn-0.5Li (AR) sample surfaces are collected. The C 1s spectra consist of five peaks centered at 284.5 eV, 285.4 eV, 286.2 eV, 287.5 eV and 288.3 eV,

which indicate C–H/C–C, C–N, C–O, C=O and O=C–N (Figs. 13c1 and 14c2)[51]. The N 1s spectra consist of two peaks centered at 399.4 eV and 400.0 eV, which indicate C–N, C=O–NH (Figs. 13d1 and 14d2)[51]. These characteristic bonds indicate the presence of BSA on sample surfaces.

Zn (AR) has a relatively smooth surface with a few flaky corrosion products (Fig. 13e1). In contrast, the surface of Zn-0.5Li (AR) is uneven, featuring numerous spherical corrosion products (Fig. 13e2). Additionally, the surface of Zn-0.5Li (AR) contains higher concentrations of C, O, and N, indicating more BSA adsorption (Fig. 13f1, f2).

Figure 14 shows COF curves of Zn (AR) and Zn-0.5Li (AR) alloys after 1 h tribocorrosion. With the addition of 10 g/L BSA, average COFs of the samples decrease to 0.47 and 0.36, respectively, corresponding to reductions of 44% and 31%. Scratch surface and cross-sectional morphologies of the samples are shown in Fig. 15. After adding BSA, scratch surface roughness of Zn (AR) and Zn-0.5Li (AR) are 4.2 ± 0.1 μm and 0.9 ± 0.8 μm, respectively, corresponding to reductions of 28% and 65% (Fig. 16b, e). Maximum widths of the scratches decrease by 12% and 26%, and maximum depths decrease by 46% and 70%, respectively (Fig. 16b, e). Due to the presence of the BSA adsorption layer, the wear area of Zn (AR) and Zn-0.5Li (AR) was reduced by 55% and 81%, respectively.

SEM images of scratch morphologies after tribocorrosion in PBS + BSA are shown in Fig. 17a, b. Zn (AR) shows many micro-scratches parallel to the sliding direction, indicating abrasive wear. No obvious fatigue cracks or spalling pits are observed on the scratch surface. In contrast, Zn-0.5Li (AR) has a narrower scratch with furrows on both sides and fine cracks in the center, indicating a combination of abrasive and fatigue wear. Figure 16c, d shows the EDS results and element concentrations. Compared to Fig. 6, the scratch surface of Zn-0.5Li (AR) shows enrichment of P and O.
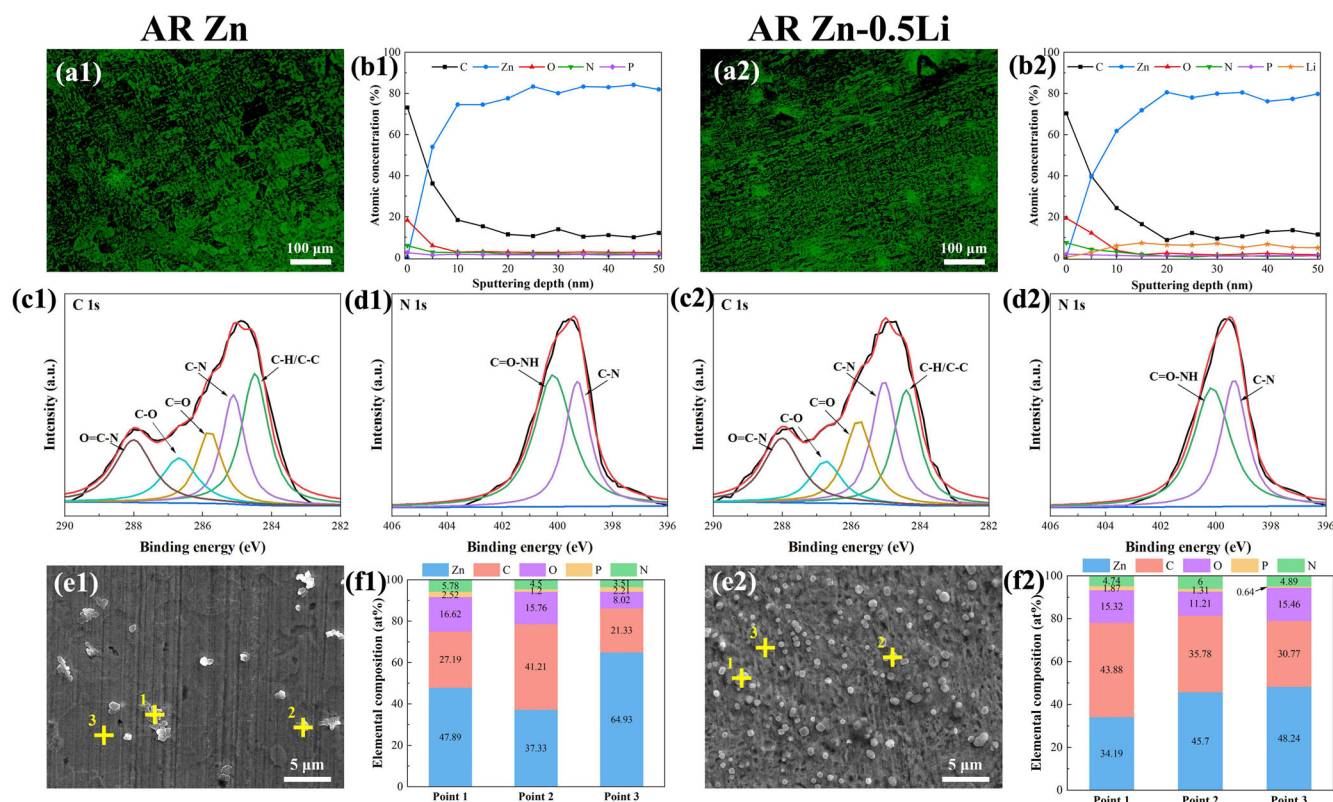
Fig. 13 | Adsorption behavior of BSA on the surfaces of Zn (AR) and Zn-0.5Li (AR). Pure Zn (AR) and Zn-0.5Li (AR) alloy immersed in PBS solution with 10 g/L BSA for 24 h: **a1**, **a2** Fluorescence microscopic morphology; **b1**, **b2** XPS element depth analysis; **c1**, **c2** high-resolution XPS spectra of C 1s; **d1**, **d2** high-resolution XPS spectra of N 1s; **e1**, **e2** surface morphology; **f1**, **f2** EDS point scan results of (**e1**, **e2**).
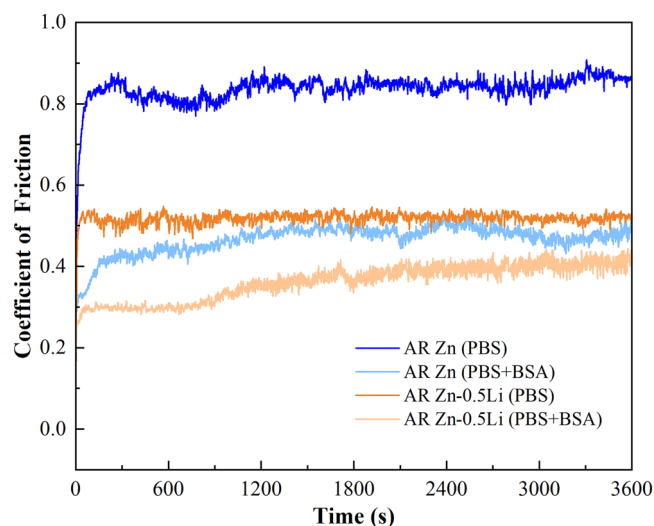

Fig. 14 | Friction coefficients of Zn (AR) and Zn-0.5Li (AR) alloy during tribo-corrosion in PBS containing BSA. COF curves of Zn (AR) and Zn-0.5Li (AR) alloy.

Discussion

After corrosion wear, contents of P and O elements on the scratch surface of Zn are significantly higher than those of the substrate on either side (Fig. 5). In contrast, the enrichment of P and O on the scratch surface of Zn-0.5Li alloy is not significant (Fig. 6). To elucidate such a difference, micro-area XPS tests are conducted on the scratch surfaces of both pure Zn and Zn-0.5Li alloy.

High-resolution XPS spectrum of pure Zn is presented in Fig. 7. The Zn $2p_{3/2}$ spectra consist of two peaks centered at 1021.9 eV and 1022.5 eV, which indicate ZnO and $ZnCO_3$, respectively. $ZnCl_2$ is also present on the scratch surface of pure Zn, with a binding energy of 1023.7 eV[52]. The fitting results of P 2p indicate that $Zn_3(PO_4)_2$ and Na_2HPO_4 are formed on the scratch surface, with binding energy peaks at 133.6 eV and 132.8 eV, respectively[53]. $Zn_3(PO_4)_2$ is virtually insoluble in water, hence it covers the scratched surface. The corrosion wear products of $ZnCl_2$ and Na_2HPO_4 are water-soluble compounds, originating from the adsorbed Cl^- and HPO_4^{2-} in PBS solution on the scratch surface.

Figure 7 shows the high-resolution XPS spectra from the scratch surface of Zn-0.5Li alloy after corrosion wear, including Zn $2p_{3/2}$, Li 1s, and P 2p. The spectra of Zn $2p_{3/2}$ indicate that the Zn-rich corrosion products are ZnO and $ZnCO_3$. The Li 1 s spectra consist of two peaks centered at 55.4 eV and 54.9 eV, which indicate Li_3PO_4 and LiOH, respectively[45]. The fitting results of P 2p demonstrate that $Zn_3(PO_4)_2$ is also present on the scratch surfaces of both Zn-0.5Li (AC) and Zn-0.5Li (AR) alloys.

Standard enthalpies of the formation of LiOH and Li_3PO_4 are −484.93 and −3383.4 kJ/mol, respectively[54]. As for $Zn_3(PO_4)_2$, ZnO and $ZnCO_3$, they are −5113.4 kJ/mol, −384.3 kJ/mol and −1081.1 kJ/mol, respectively[45]. Therefore, as a lower enthalpy value indicates a greater chemical stability, their thermodynamic stabilities can be ranked decreasingly as follows: $Zn_3(PO_4)_2 > Li_3PO_4 > ZnCO_3 > LiOH > ZnO$. So $Zn_3(PO_4)_2$ and Li_3PO_4 should be more stable than the others.

Due to wear-induced acceleration of corrosion, formation of $Zn_3(PO_4)_2$ on the scratch of pure Zn is promoted, resulting in an enrichment of P and O elements (Fig. 5). As for Zn-0.5Li alloy, the distribution of corrosion products containing P element, namely $Zn_3(PO_4)_2$ and Li_3PO_4, shows no significant difference (Fig. 6). This indicates that there is no evidence of wear-induced promotion of corrosion on the scratch of the alloy. Comparative analysis reveals that the presence of Li_3PO_4 in the corrosion product layer renders it compact, thereby enhancing its resistance to corrosion wear. A similar result has been observed upon immersion of Zn-0.8Li alloy in simulated body fluid. A corrosion product layer of polycrystalline
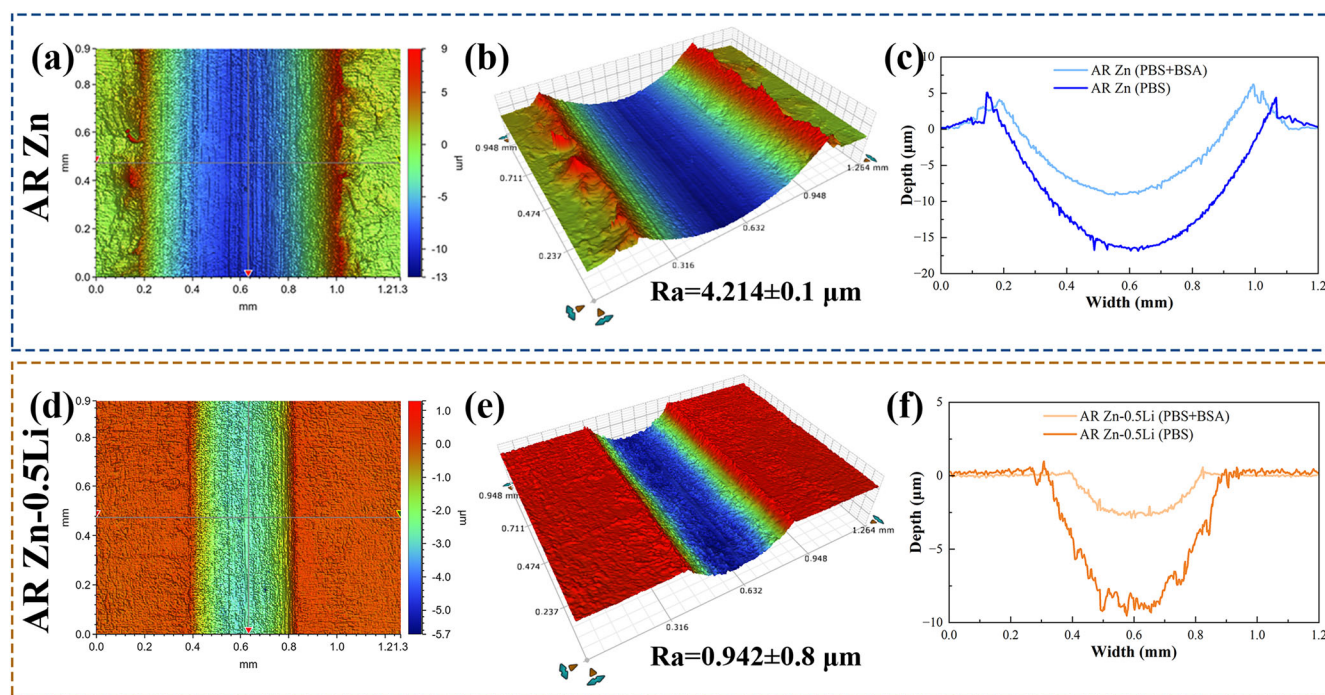
Fig. 15 | Scratch morphology of Zn (AR) and Zn-0.5Li (AR) after 1 h of tribocorrosion in PBS solution with 10 g/L BSA. a, b, d, e Scratch appearances, **c, f** cross-sectional morphologies.

Li_2CO_3 forms on the alloy's surface, effectively suppressing pitting corrosion[55].

Enhancement of corrosion on wear is predominantly exhibited through the following mechanisms: (1) Corrosion induces formation of pits and corrosion products on a material's surface, which augments surface roughness; (2) Corrosion weakens binding strengths of grain and phase boundaries[26]. Corrosion predominantly causes dissolution of the alloy matrix, exposing second-phase particles on the material's surface[3]. These particles are prone to being detached under impact and collision with frictional counterparts, resulting in wear mass loss.

Enhancement of wear on corrosion is predominantly exhibited through the following mechanisms: (1) Wear disrupts the passive film on the material's surface, establishing a galvanic couple between the scratch and the surrounding area. The scratch acts as an anode and thus accelerates dissolution[56]. (2) Wear accelerates the flow of the solution environment, facilitating a more rapid response of depolarizers to the scratch. (3) Wear induces plastic deformation on the material's surface, resulting in the formation of microcracks and an increase in defects such as dislocations and vacancies. These enhance the reactivity of the scratch surface and intensify corrosion[20].

Based on OCP and potentiostatic test results (Fig. 11), calculations are performed for each component of the corrosion wear process using the interaction formulas introduced in methods section. The results are presented in Tables 4 and 5; proportions of each component are then depicted in pie charts (Fig. 17).

Figure 18 shows the mechanism of corrosive wear behavior and the mechanism of Zn-0.5Li (AR) alloy in PBS under different potentials. When tested under the cathodic protection potential (−1.3 V), the current density is negative owing to the cathodic reduction reaction of dissolved oxygen. The power source provides electrons. The working electrodes (i.e., pure Zn and Zn-0.5Li alloy) act as the cathode, where the following reaction occurs:

$$O_2 + 2H_2O + 4e^- \rightarrow 4OH^- \qquad (2)$$

The loss of both metals is entirely due to abrasive wear in the absence of corrosion. The cathodic current increases during wear, due to a larger oxygen reduction rate resulting from accelerated mass transport by the stirring of solution[26]. The total material loss rate (T) is equivalent to the pure wear rate (W_0). W_0 values of Zn (AR) and Zn-0.5Li (AR) alloy are 22.34 mm/year and 4.76 mm/year, respectively. After wear, the current reached the initial level (Fig. 12b).

Under self-corrosion potential (i.e., OCP, −1.1 V), corrosion has taken effect, which differs from the −1.3 V situation. Wear rate increments caused by corrosion (ΔW_c) of Zn (AR) and Zn-0.5Li (AR) alloy are 20.79 mm/year and 33.82 mm/year, which account for 47.08% and 84.42% of the total material loss rate, respectively (second column of Fig. 17). The remainder corresponds to corrosion rate increment caused by wear (ΔC_w), which account for 2.31% and 2.54%, respectively. Passive film is removed by wear, exposing a fresh metal surface. Galvanic corrosion is formed between scratch and the surrounding metal substrate, causing the current density to increase continually during wear (Fig. 12c). It should be noted that the material loss of the alloy is primarily due to the ΔW_c. The potential of the alloy is lower during corrosion wear (Fig. 12a), which suggests a poorer corrosion resistance[44]. Corrosion pits can be observed in the scratch of the alloy in spite of −1.1 V is below its pitting potential of −0.7 V (Figs. 10 and 12). This is due to the micro-galvanic corrosion between Zn and β-LiZn$_4$. The current density curve of the alloy in Fig. 12c exhibits noticeable fluctuations during the wear process, indicating the occurrence of meta-stable pitting characterized by nucleation-death of active sites[57]. Pitting corrosion inside the scratch (Fig. 11h) promotes surface crack propagation and leads to corrosion-accelerated wear in modes of abrasive, adhesive, and fatigue (Fig. 11h). In the vicinity of the crack tips, defects such as dislocations and vacancies accelerate corrosion. As a result, the detachment of material from the scratch surface becomes more facile, leading to an increase in ΔW_c.

Under anodic corrosion potential (−0.9 V), current density during wear is larger compared to other potential conditions (Fig. 12d). In Zn (AR) and Zn-0.5Li (AR) alloy, ΔC_w are 16.41 mm/year and 24.52 mm/year, which account for 22.77% and 36.50% of the total material loss rate, respectively (third column of Fig. 17). The proportion of ΔC_w expands, comparing to the −1.1 V condition. Under anodic potentials, the metal surface is more inclined to lose electrons, thereby facilitating the occurrence of oxidation reactions[56]. After wear, the current density values of both metals do not
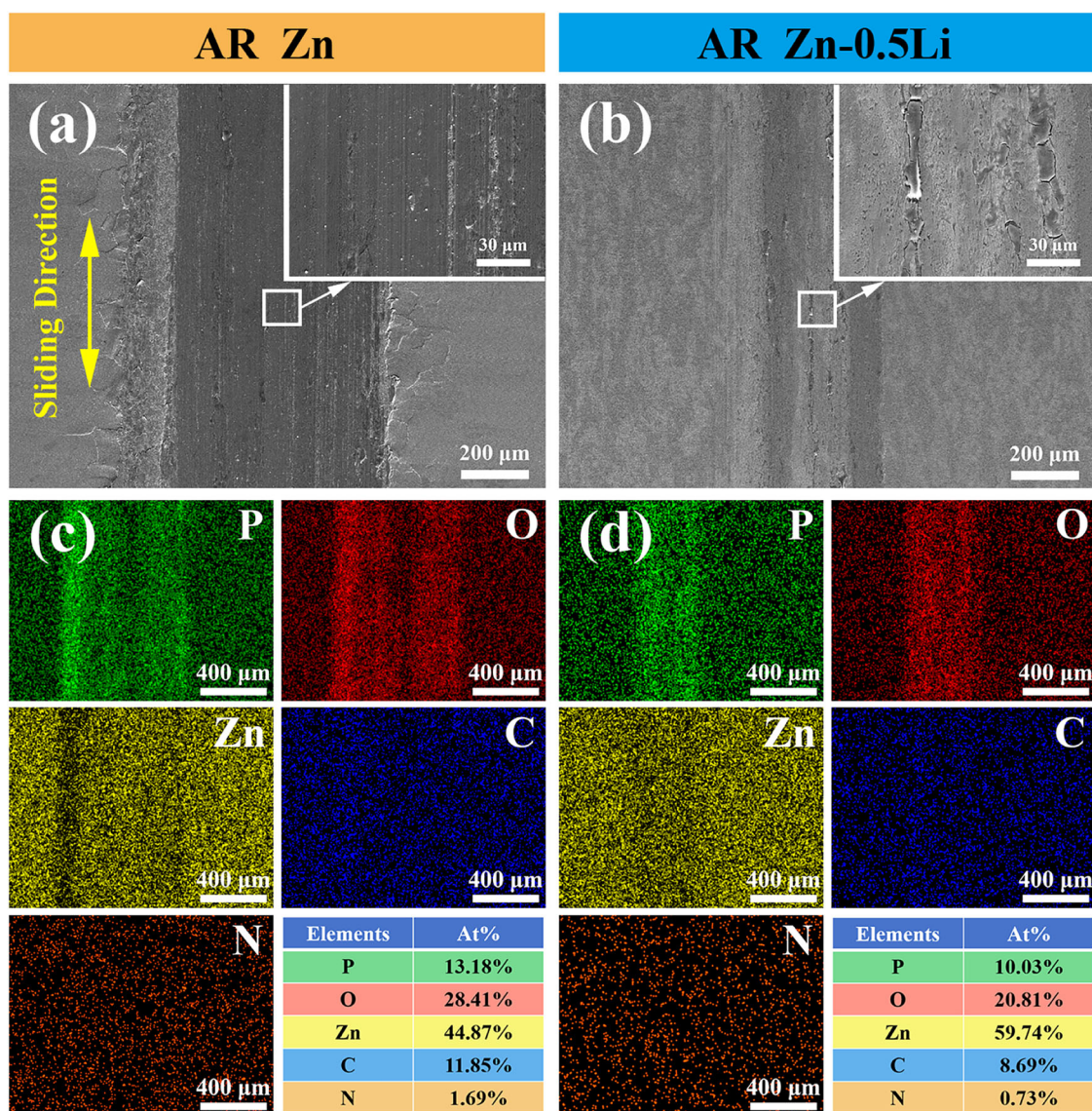
Fig. 16 | Micro-morphology and elemental distribution of the scratches on Zn (AR) and Zn-0.5Li (AR) alloy after 1 h tribocorrosion in PBS solution with 10 g/L BSA. a, **b** SEM of scratch, **c**, **d** EDS results and proportion of each element.

revert to their initial values rapidly (Fig. 12d). This may be due to the following reasons: (1) At the anodic corrosion potential, the repassivation of the passive film is slow, keeping the surface in an active state; (2) The corrosion products covering the metal surface are not promptly carried away by the solution, hindering the repair of the passive film. Additionally, the more severe tribocorrosion under OCP and anodic potentials can also be explained by the concept of tribolayers. The tribolayer is a dynamically adhered layer encapsulated by wear debris and corrosion products[44]. During tribocorrosion, micro-cracks and plastic deformation cause surface delamination. The detached debris is re-pressed onto the surface under normal load and electrochemical interactions, forming oxygen- and phosphorus-enriched tribolayers (as shown in Figs. 5 and 6). When tribolayers detach, their hard particles act as "third bodies," triggering three-body abrasive wear that exacerbates spalling and groove damage[44]. Anodic potential intensifies substrate oxidation, promoting more oxidized debris generation and thus enhancing tribolayer formation. However, it simultaneously reduces tribolayer adhesion, accelerating detachment and significantly increasing the contribution of three-body wear[44]. This explains the abnormally high wear rate of Zn-0.5Li alloy under high potentials.

As shown in Fig. 13, more BSA is adsorbed on Zn-0.5Li (AR), forming a thicker layer than on pure Zn (AR). As a charged biomacromolecule, BSA is capable of binding charged active sites of metal surfaces[58]. Addition of Li changes the electron cloud distribution of Zn, creating more uncoordinated electron regions (i.e., active sites)[59]. Meanwhile, formation of LiZn$_4$ introduces defects (e.g., vacancies), which alter surface energy and charge distribution of the alloy[60]. Surface defects increase interfacial energy, creating highly active sites that enhance hydrogen bonding and electrostatic interactions between the hydrophilic groups of BSA (such as carboxyl groups) and the metal surface[59]. Changes in electronic structure (such as increased surface negative charge due to charge transfer) weaken the electrostatic repulsion between BSA (isoelectric point pH 4.7) and the surface[60]. Both of them provide new binding sites for BSA. Additionally, Li$^+$ ions can engage in electrostatic interactions with the charged amino acid residues in BSA[60]. Therefore, Zn-0.5Li alloy exhibits superior BSA adsorption performance compared to pure Zn.

After adding 10 g/L BSA, tribocorrosion of Zn-0.5Li (AR) alloy is significantly alleviated, with the wear area decreasing by 81% (Fig. 15). The mechanism of this alleviating effect can be divided into two parts: (1) reducing wear through lubrication and (2) protecting Zn substrate from galvanic corrosion. As shown in Figs. 6 and 17, adhesive wear, which typically occurs under high COF and poor lubrication conditions, is no longer observed on the alloy surface after adding BSA. BSA molecules
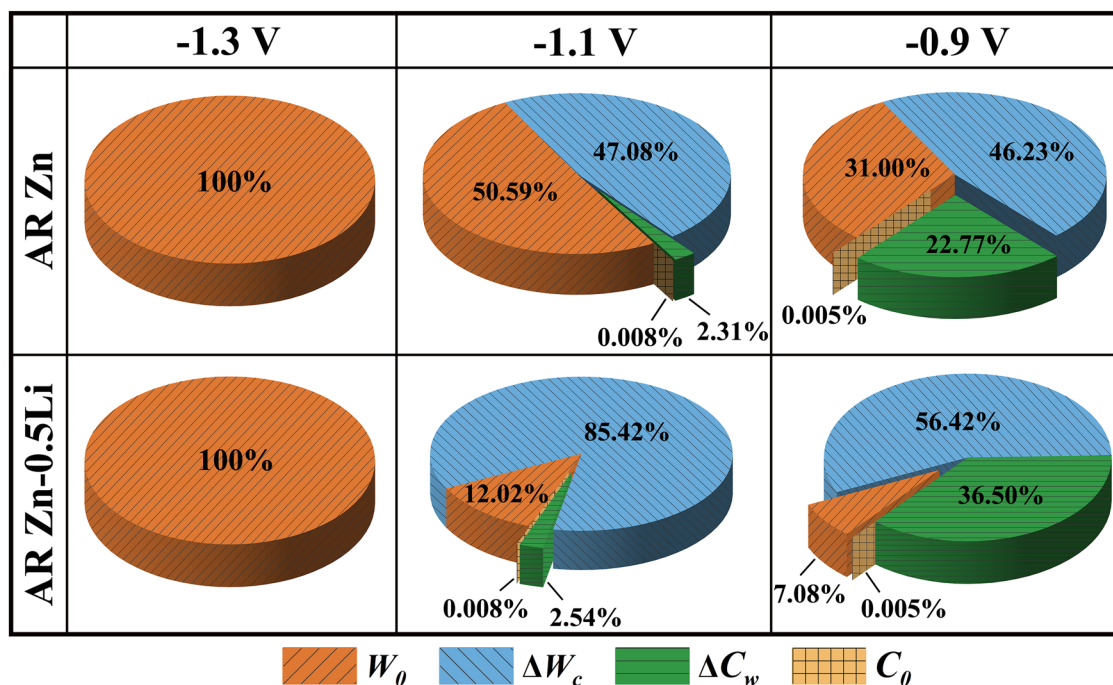
Fig. 17 | Proportional distribution of the interaction components of corrosion wear for Zn (AR) and Zn-0.5Li (AR) alloy at different potentials in PBS solution. W_0 represents wear rate in the absence of corrosion, C_0 represents pure corrosion rate in the absence of wear, ΔW_c represents wear rate increments caused by corrosion, ΔC_w represents corrosion rate increments caused by wear.
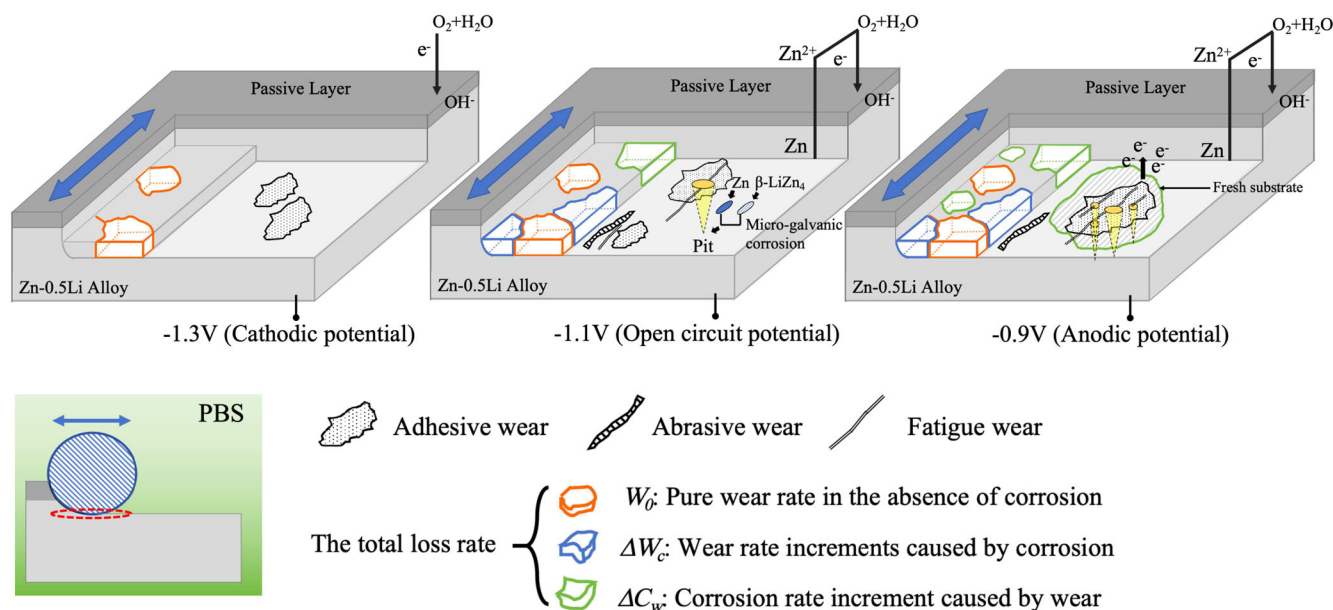

Fig. 18 | Schematic diagram of the evolution process of the scratch surface of Zn-0.5Li (AR) alloy during corrosion wear under different potentials. Under the cathodic protection potential (-1.3 V), the loss of both metals is entirely due to abrasive wear in the absence of corrosion. Under self-corrosion potential (i.e., OCP, -1.1 V), corrosion has taken effect. Under anodic corrosion potential (-0.9 V), current density during wear is larger compared to other potential conditions.

possess flexibility and lubricity, and their adsorption layer can act as a cushion and lubricant between two contacting surfaces. As a result, the COF is reduced and tribocorrosion is alleviated (Figs. 14 and 16). BSA absorption can also reduce the tribocorrosion effect by alleviating galvanic corrosion between the scratch and its neighboring unworn regions[44]. During tribo-corrosion, the BSA layer is worn away first, and the corrosion product layer containing Li_3PO_4 and $Zn_3(PO_4)_2$ will re-form quickly after wear (Fig. 19a). Therefore, compared to the unworn regions that are still covered by

BSA, there is a significant enrichment of P and O on the scratch's surface (Fig. 16).

Figure 19b illustrates the impact of adding 10 g/L BSA on the wear area of pure Zn (AR), Zn-0.5Li (AR) alloy, and Zn-0.4Mn alloy we previously studied[44]. Both alloys demonstrate superior wear resistance compared to pure Zn. After adding BSA, wear areas of the alloys decrease by 81% and 72%, respectively. Different alloying elements have different effects on BSA adsorption. However, this area is under-researched, and it is highly
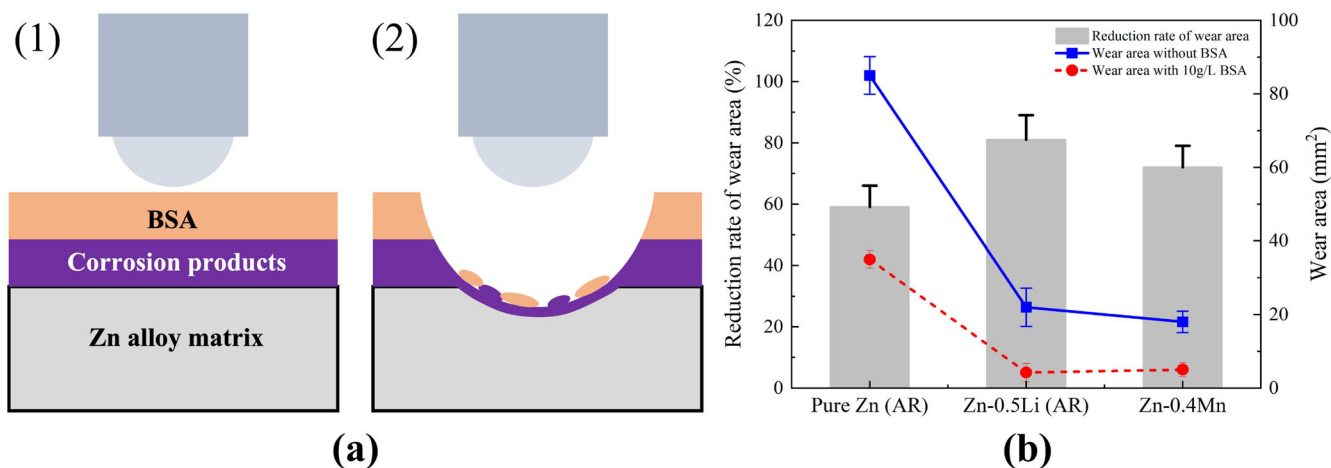
Fig. 19 | Influence of BSA on the tribocorrosion behavior of Zbn-0.5Li (AR) alloy and its underlying mechanism. a Schematic diagram of the scratch surface of Zn-0.5Li (AR) alloy during tribocorrosion. **b** Change in wear area of pure Zn and Zn alloys after addition of 10 g/L BSA. Data of Zn-0.4Mn in (**b**) come from the ref. 44.

Table 4 | Calculation of the interaction components of corrosion wear of Zn (AR) in PBS solution at different potentials

Potential (V)	ΔV ($\times 10^{-2}$ mm^3)	s (mm^2)	t (h)	i_0 (μA/cm^2)	i_w ($\times 10^3$ μA/cm^2)	T (mm/year)	C (mm/year)	W_0 (mm/year)	C_0 (mm/year)	ΔW_c (mm/year)	ΔC_w (mm/year)
−1.3	1.32	10.35	0.5	0.24	0	22.34	0	22.34	0	0	0
−1.1	3.32	13.17	0.5	0.24	0.07	44.16	1.026	22.34	0.0035	20.79	1.022
−0.9	6.22	15.12	0.5	0.24	1.12	72.07	16.414	22.34	0.0035	33.32	16.411

ΔV represents wear volume change, s represents wear scratch area, t represents wear time, i_0 represents corrosion current density under static corrosion, i_w represents corrosion current density under corrosion wear, T represents total material loss rate, C represents total electrochemical corrosion rate, W_0 represents wear rate in the absence of corrosion, C_0 represents pure corrosion rate in the absence of wear, ΔW_c represents wear rate increment caused by corrosion, ΔC_w represents corrosion rate increment caused by wear, i_0 is I_{corr} in Section 3.4.1, $C = C_0 + \Delta C_w$.

Table 5 | Calculation of interaction components of corrosion wear of Zn-0.5Li (AR) in PBS solution at different potentials

Potential (V)	ΔV ($\times 10^{-2}$ mm^3)	s (mm^2)	t (h)	i_0 (μA/cm^2)	i_w ($\times 10^3$ μA/cm^2)	T (mm/year)	C (mm/year)	W_0 (mm/year)	C_0 (mm/year)	ΔW_c (mm/year)	ΔC_w (mm/year)
−1.3	0.11	4.05	0.5	0.22	0	4.76	0	4.76	0	0	0
−1.1	1.88	8.32	0.5	0.22	0.07	39.59	1.010	4.76	0.0032	33.82	1.007
−0.9	4.59	11.97	0.5	0.22	1.70	67.18	24.525	4.76	0.0032	37.90	24.522

Table 6 | Compositional analysis of Zn-0.5Li alloy

No.	Samples	Li (wt.%)	Zn (wt.%)
1	Zn	0	Bal.
2	Zn-0.5Li	0.57	Bal.

significant for the development of biodegradable Zn alloys with anti-tribocorrosion properties.

Methods
Alloys preparation
Raw materials of pure Zn (99.95 wt.%) and Li (99.95 wt.%) were received from General Research Institute for Nonferrous Metals, Beijing, China. They were weighed according to nominal alloy composition of Zn-0.5Li, and then melted in a vacuum induction melting furnace under the atmosphere of Ar protection. After being kept at 750 °C for 2 min, the melt was cast into a steel die. The actual composition of the alloy was measured to be Zn-0.57Li through inductively coupled plasma atomic emission spectrometry (ICP-AES, Leeman Labs, USA), with the results presented in Table 6.

The ingot was homogenized first at 250 °C for 2 h and then at 350 °C for 2 h, followed by furnace cooling.

Rolling blanks of $40 \times 35 \times 20$ mm were cut from the ingots, and hot rolled at 350 °C to a final thickness of 5 mm through three passes. The deductions of the three passes were 15%, 17.6% and 21.4% in sequence. Subsequently, the blanks were tempered at 350 °C for 15 min, followed by two passes of rolling with reductions of 27.3% and 37.5%, resulting in a total reduction of 75%. The hot-rolled plates were quenched in cool water, heated at 200 °C for 30 min, and then warm rolled at 200 °C to 2 mm in thickness through a single pass, with a large reduction of 60%. After the warm rolling, the plates were again quenched in cool water.

Characterization of microstructure
Phases in the alloy were analyzed by XRD (Smart Lab 9 kW, Rigaku, Japan) with CuK$_\alpha$ radiation with 2θ from 20° to 90° at a scanning rate of 5°/min. Surface morphology was observed using a white light interferometer (WLI, Contour GTK, German). Microstructure was observed by using an SEM (Regulus 8100, Japan). All SEM images were acquired in secondary electron mode to prioritize topographical features of corroded surfaces.
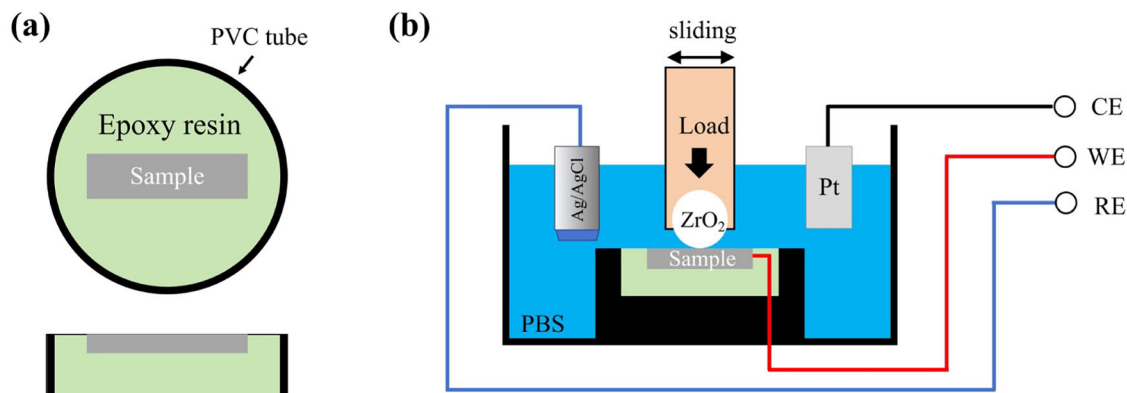
Fig. 20 | Schematic diagram of the tribocorrosion test. a Tribocorrosion test sample morphology; **b** measurement setup of tribocorrosion test.

Mechanical property tests

Hardness testing was carried out by using a VTD512 micro-Vickers hardness tester (Leica, Germany) according to standard GB/T 4340.1-2009. Tensile mechanical testing was performed on a WDW-10E/20E electronic universal testing machine with a tensile rate of 1 mm/min, at room temperature. Three parallel samples were tested.

Electrochemical tests

Electrochemical measurements were performed by an electrochemical analyzer (ModuLab XM). A three-electrode cell setup was used wherein the Zn-0.5Li samples, saturated calomel electrode (SCE), and a platinum sheet were used as the working, reference, and counter electrodes, respectively. OCP measurements were recorded for 1800s immersion. Potentiodynamic polarization (PDP) tests were conducted in a range of -1.5 to -0.5 V vs. SCE at a constant scan rate of 1 mV/s. EIS studies were carried out at OCP of 5 mV sinusoidal amplitude in the frequency range of 10^5 Hz to 10^{-2} Hz. The anodic corrosion potential, self-corrosion potential, and cathodic protection potential in the electrochemical experiment of corrosion wear were determined according to the polarization curve.

Tribocorrosion tests

The Zn and Zn-0.5Li blanks of $20 \times 5 \times 2$ mm were cut and embedded using an epoxy resin in a polyvinyl chloride tube. All the samples were divided into two groups and immersed in PBS, and investigated by a tribometer (Bruker UMT, USA). To one group, BSA was added concentration of 10 g/L to make it closer to the concentration of albumin in human joint fluid. The applied load was 5 N, the reciprocating frequency was 1 Hz, and the testing period was 1 h. The schematic diagram of the experiment is shown in Fig. 20. During the experiment, the tribometer will automatically record the COF. Triplicate measurements were performed for each sample in tribocorrosion tests.

The morphology of the wear scratch was observed using an SEM. The surface composition of the wear scratch was gained using XPS. The three-dimensional morphology of the wear track was observed with a WLI, and the wear loss volume was calculated:

$$\Delta V = SL \tag{3}$$

Where ΔV is the volume of wear (mm³), S is the cross-sectional area of the wear track (mm²), and L is the sliding distance (mm).

The tribocorrosion experimental setup was connected to the electrochemical three-electrode system. PBS was then added, and tribocorrosion tests were conducted under constant potential. The tests were performed under cathodic potential, OCP, and anodic potential, respectively. The cathodic potential condition was used to measure the tribocorrosion behavior of the alloy under pure wear conditions. The OCP condition simulated the tribocorrosion behavior under normal service conditions. The anodic potential condition assessed the tribocorrosion behavior in severely corrosive environments.

Calculation of wear/corrosion interaction

According to ASTM G119-09, the interactive effects of metal corrosion and wear can be quantitatively analyzed by calculating the following parameters. The total loss rate T (mm/year) of material consists of three parts: the wear rate in the absence of corrosion W_0 (mm/year), the electrochemical corrosion rate C_0 (mm/year), and the material loss rate S (mm/year) caused by the interaction of corrosion and wear, as shown in Eq. (4):

$$T = W_0 + C_0 + S \tag{4}$$

The interactive action loss rate S includes the increment of corrosion ΔC_w caused by wear and the increment of wear ΔW_c caused by corrosion, as shown below:

$$S = \Delta C_w + \Delta W_c \tag{5}$$

$$T = W_0 + C_0 + \Delta C_w + \Delta W_c \tag{6}$$

The total wear rate W and the total corrosion rate C in the total loss rate T were calculated according to the following equations:

$$W = W_0 + \Delta W_c \tag{7}$$

$$C = C_0 + \Delta C_w \tag{8}$$

T and W_0 were calculated as follows:

$$T = \frac{m_0 - m_1}{s\rho t} = \frac{\Delta V}{st} \tag{9}$$

$$W_0 = \frac{m_0 - m_2}{s\rho t} = \frac{\Delta V}{st} \tag{10}$$

where m_0 (mg) is the initial mass of the sample; m_1 (mg) is the remnant mass of the sample after tribocorrosion test; m_2 (mg) is the final mass of the sample after the cathodic protection experiment; ρ (g/cm³) is the density of the material; s (mm²) is the wear track area of the sample; t (h) is the duration of the wear test.

According to ASTM G95-23, the total corrosion rate C (mm/year) and the electrochemical corrosion rate C_0 (mm/year) are calculated according to

the following equations:

$$C_0 = 3.27 \times 10^{-3} \frac{i_0}{\rho} EW \quad (11)$$

$$C = 3.27 \times 10^{-3} \frac{i_w}{\rho} EW \quad (12)$$

$$EW = \frac{1}{\sum \frac{n_i f_i}{w_i}} \quad (13)$$

where i_0 (μA/cm^2) and i_w (μA/cm^2) represent corrosion current density under static corrosion and tribocorrosion. EW (g) is the equivalent weight, where n_i represents the valence of the ith element of the alloy, f_i represents the mass fraction of the ith element in the alloy, and W_i represents the atomic mass of the ith element in the alloy.

Data availability
The raw data can be shared on request.

References
1. Yin, S. & Li, D. Y. A new phenomenon observed in determining the wear-corrosion synergy during a corrosive sliding wear test. *Tribol. Lett.* **29**, 45–52 (2008).
2. Mathew, M. T., Jacobs, J. J. & Wimmer, M. A. Wear-corrosion synergism in a CoCrMo hip bearing alloy is influenced by proteins. *Clin. Orthop. Relat. Res.* **470**, 3109–3117 (2012).
3. Xu, W. et al. Synergistic interactions between wear and corrosion of Ti-16Mo orthopedic alloy. *J. Mater. Res. Technol.* **9**, 9996–10003 (2020).
4. Yakupov, N. M. & Yakupov, S. N. Corrosion wear under vibrations. *Dokl. Phys.* **63**, 147–149 (2018).
5. Mischler, S. & Muoz, A. I. Wear of CoCrMo alloys used in metal-on-metal hip joints: a tribocorrosion appraisal. *Wear* **297**, 1081–1094 (2013).
6. Yan, Y., Neville, A. & Dowson, D. Biotribocorrosion of CoCrMo orthopaedic implant materials—assessing the formation and effect of the biofilm. *Tribol. Inter.* **40**, 1492–1499 (2007).
7. Barril, S., Mischler, S. & Landolt, D. Influence of fretting regimes on the tribocorrosion behaviour of Ti6Al4V in 0.9wt.% sodium chloride solution. *Wear* **256**, 963–972 (2004).
8. Namus, R. & Rainforth, W. M. Influence of protein adsorption on tribocorrosion behaviour of CoCrMo biomedical-grade alloys. *Tribol. Int.* **150**, 106364 (2020).
9. Xu, L. et al. Corrosion and tribocorrosion protection of AZ31B Mg alloy by a hydrothermally treated PEO/chitosan composite coating. *Prog. Org. Coat.* **170**, 107002 (2022).
10. Yan, Y., Yang, H., Su, Y. & Qiao, L. Study of the tribocorrosion behaviors of albumin on a cobalt-based alloy using scanning Kelvin probe force microscopy and atomic force microscopy. *Electrochem. Commun.* **64**, 61–64 (2016).
11. Akazawa, T. et al. Corrosion of spinal implants retrieved from patients with scoliosis. *J. Orthop. Sci.* **10**, 200–205 (2005).
12. Barril, S., Debaud, N., Mischler, S. & Landolt, D. A tribo-electrochemical apparatus for in vitro investigation of fretting–corrosion of metallic implant materials. *Wear* **252**, 744–754 (2002).
13. Eltit, F. et al. Adverse reactions to metal on polyethylene implants: Highly destructive lesions related to elevated concentration of cobalt and chromium in synovial fluid. *J. Biomed. Mater. Res.* **105**, 1876–1886 (2017).
14. Prakasam, M. et al. Biodegradable materials and metallic implants—a review. *J. Funct. Biomater*. **8**, https://doi.org/10.3233/thc-2012-0685 (2017).
15. Yang, H. et al. Alloying design of biodegradable zinc as promising bone implants for load-bearing applications. *Nat. Commun.* **11**, 401 (2020).
16. Gilbert, J. L., Buckley, C. A. & Jacobs, J. J. In vivo corrosion of modular hip prosthesis components in mixed and similar metal combinations. The effect of crevice, stress, motion, and alloy coupling. *J. Biomed. Mater. Res.* **27**, 1533–1544 (1993).
17. Wang, S., Liao, Z. H., Feng, P. F. & Liu, W. Q. Research progress on biotribocorrosion of metal material in orthopedic implants. *Tribology* **37**, 130–138 (2017).
18. Wang, K. et al. Binary Zn–Ti alloys for orthopedic applications: corrosion and degradation behaviors, friction and wear performance, and cytotoxicity. *J. Mater. Sci. Technol.* **74**, 216–229 (2021).
19. Wang, T. et al. In vitro performance of a biodegradable zinc alloy adjustable-loop cortical suspension fixation for anterior cruciate ligament reconstruction. *Int. J. Miner. Metall. Mater.* **31**, 887–898 (2024).
20. Zhu, D., Liu, Y. & Gilbert, J. L. In vitro fretting crevice corrosion damage of CoCrMo alloys in phosphate buffered saline: debris generation, chemistry and distribution. *Acta Biomater.* **114**, 449–459 (2020).
21. Uchihara, Y. et al. Implant failure in bilateral metal-on-metal hip resurfacing arthroplasties: a clinical and pathological study. *J. Mater. Sci. Mater.* **29**, 28 (2018).
22. Su, Y. et al. Enhanced cytocompatibility and antibacterial property of zinc phosphate coating on biodegradable zinc materials. *Acta Biomater.* **98**, 174–185 (2019).
23. Voggenreiter, G. et al. Immuno-inflammatory tissue reaction to stainless-steel and titanium plates used for internal fixation of long bones. *Biomaterials* **24**, 247–254 (2003).
24. Gilbert, J. L., Mali, S., Urban, R. M., Silverton, C. D. & Jacobs, J. J. In vivo oxide-induced stress corrosion cracking of Ti-6Al-4V in a neck–stem modular taper: Emergent behavior in a new mechanism of in vivo corrosion. *J. Biomed. Mater. Res. B Appl. Biomater.* **100**, 584–594 (2012).
25. Huang, X. et al. Crevice corrosion behaviors of CoCrMo alloy and stainless steel 316L artificial joint materials in physiological saline. *Corros. Sci.* **197**, 110075 (2022).
26. Ren, P., Meng, H., Xia, Q., Zhu, Z. & He, M. Tribocorrosion of 316L stainless steel by in-situ electrochemical methods under deep-sea high hydrostatic pressure environment. *Corros. Sci.* **202**, 110315 (2022).
27. Xiao, C. et al. Indirectly extruded biodegradable Zn-0.05wt%Mg alloy with improved strength and ductility: in vitro and in vivo studies. *J. Mater. Sci. Technol.* **34**, 1618–1627 (2018).
28. Song, Y., Yuan, K., Li, X. & Qiao, Y. Microstructure and properties of biomedical Mg-Zn-Ca alloy at different extrusion temperatures. *Mater. Today Commun.* **35**, 105578 (2023).
29. Shuai, C. et al. Stress-induced dual-phase structure to accelerate degradation of the Fe implant. *ACS Biomater. Sci. Eng.* **8**, 1841–1851 (2022).
30. Goldberg, J. R. & Gilbert, J. L. Electrochemical response of CoCrMo to high-speed fracture of its metal oxide using an electrochemical scratch test method. *J. Biomed. Mater. Res.* **37**, 421–431 (1997).
31. Yin, S. et al. Effects of Zn/Gd ratio on the microstructures and mechanical properties of Mg-Zn-Gd-Zr alloys. *Mater. Sci. Eng. A* **695**, 135–143 (2017).
32. Yin, Y. X. et al. Hemocompatibility of biodegradable Zn-0.8 wt% (Cu, Mn, Li) alloys. *Mater. Sci. Eng. C Mater. Biol. Appl.* **104**, 109896 (2019).
33. Tang, Z. et al. Potential biodegradable Zn-Cu binary alloys developed for cardiovascular implant applications. *J. Mech. Behav. Biomed. Mater.* **72**, 182–191 (2017).

34. Shi, Z. Z., Li, M., Li, X. M. & Wang, L. N. Surface-roughness-induced plasticity in a biodegradable Zn alloy. *Adv. Mater.* **35**, e2207570 (2023).

35. Jia, B. et al. Biodegradable Zn–Sr alloy for bone regeneration in rat femoral condyle defect model: in vitro and in vivo studies. *Bioact. Mater.* **6**, 1588–1604 (2021).

36. Mao, G. et al. Effect of biodegradable Zn screw on bone tunnel enlargement after anterior cruciate ligament reconstruction in rabbits. *Mater. Des.* **207**, 109834 (2021).

37. Vojtěch, D., Kubásek, J., Šerák, J. & Novák, P. Mechanical and corrosion properties of newly developed biodegradable Zn-based alloys for bone fixation. *Acta Biomater.* **7**, 3515–3522 (2011).

38. Katarivas Levy, G., Goldman, J. & Aghion, E. The prospects of zinc as a structural material for biodegradable implants—a review paper. *Metals* **7**, 402 (2017).

39. Guillory, R. J. et al. Improved biocompatibility of Zn–Ag-based stent materials by microstructure refinement. *Acta Biomater.* **145**, 416–426 (2022).

40. Li, H., Huang, Y., Ji, X., Wen, C. & Wang, L.N. Fatigue and corrosion fatigue behaviors of biodegradable Zn-Li and Zn-Cu-Li under physiological conditions. *J. Mater. Sci. Technol.* **131**, 48–59 (2022).

41. Yang, H. et al. Zn-0.4Li alloy shows great potential for the fixation and healing of bone fractures at load-bearing site. *Chem. Eng. J.* **417**, 129317 (2021).

42. Li, W., Dai, Y., Zhang, D. & Lin, J. Biodegradable Zn–0.5Li alloys with supersaturated solid solution—aging treatment for implant applications. *J. Mater. Res. Technol.* **24**, 9292–9305 (2023).

43. Sun, J.-L. et al. Biodegradable Zn-0.5Li alloy rib plate: Processing procedure development and in vitro performance evaluation. *J. Mater. Sci. Technol.* **141**, 245–256 (2023).

44. Li, B.-Y., Shi, Z.-Z., Geng, W.-B., Yan, Y. & Wang, L.N. Effect of bovine serum albumin on immersion corrosion and tribocorrosion behavior of Zn-0.4Mn alloy in simulated body fluid. *Corros. Sci.* **235**, 112165 (2024).

45. Li, Z. et al. Insight into role and mechanism of Li on the key aspects of biodegradable ZnLi alloys: microstructure evolution, mechanical properties, corrosion behavior and cytotoxicit. *Mater. Sci. Eng. C Mater. Biol. Appl.* **114**, 111049 (2020).

46. Varenberg, M. Adjusting for running-in: extension of the Archard Wear Equation. *Tribol. Lett.* **70**, 59 (2022).

47. Song, T. et al. Improvement of corrosion and wear resistance of novel Zr-Ti-Al-V alloy with high strength and toughness by thermal nitridation treatment. *Corros. Sci.* **208**, 110685 (2022).

48. Benincá, F. P. et al. Evolution of morphology, microstructure and hardness of bodies and debris during sliding wear of carbon steels in a closed tribosystem. *Wear* **523**, 204809 (2023).

49. Yang, X. & Hutchinson, C. R. Corrosion-wear of β-Ti alloy TMZF (Ti-12Mo-6Zr-2Fe) in simulated body fluid. *Acta Biomater.* **42**, 429–439 (2016).

50. Salehi, E., Naderi, R. & Ramezanzadeh, B. Synthesis and characterization of an effective organic/inorganic hybrid green corrosion inhibitive complex based on zinc acetate/Urtica Dioica. *Appl. Surf. Sci.* **396**, 1499–1514 (2017).

51. Liu, L., Lu, L., Zhang, H.-J. & Wang, L.N. Influence of bovine serum albumin on corrosion behaviour of pure Zn in phosphate buffered saline. *J. Mater. Sci. Mater. Med.* **32**, 95 (2021).

52. Gmati-Ben Khaled, H., Khattech, I. & Jemal, M. Standard enthalpy of formation of lithium diphosphate. *J. Chem. Thermodyn.* **63**, 11–16 (2013).

53. Li, Z. et al. Suppression mechanism of initial pitting corrosion of pure Zn by Li alloying. *Corros. Sci.* **189**, 109564 (2021).

54. Zhang, X., Dai, J., Zhang, J. & Bai, Y. Quantitative evaluation of the interaction between wear and corrosion on Mg-3Gd-1Zn alloy in simulated body fluid. *J. Mater. Eng. Perform.* **28**, 355–362 (2019).

55. Gao, Y. et al. Effect of mechanical loading on osseointegration combined with degradation behavior of magnesium bone screw in *vivo*. *Appl. Mater. Today* **32**, 101793 (2023).

56. Jiang, J., Stack, M. M. & Neville, A. Modelling the tribo-corrosion interaction in aqueous sliding conditions. *Tribol. Int.* **35**, 669–679 (2002).

57. Htwe, E. E. et al. Adsorption characteristics of various proteins on a metal surface in the presence of an external electric potential. *Colloids Surf. B Biointerfaces* **166**, 262–268 (2018).

58. Dong, C. et al. ZnO/ZnS heterostructure with enhanced interfacial lithium absorption for robust and large-capacity energy storage. *Energy Environ. Sci.* **15**, 4738–4747 (2022).

59. Zhou, C. et al. Electrode/Electrolyte optimization-induced double-layered architecture for high-performance aqueous zinc-(dual) halogen batteries. *Nano Micro Lett.* **17**, 58 (2024).

60. Wang, C. et al. A bioinspired coating for stabilizing Li metal batteries. *ACS Appl. Mater. Interfaces* **14**, 43886–43896 (2022).

Acknowledgements

Author contributions

L.N. Wang: conceptualization, writing—review and editing, supervision. Z.Z. Shi: conceptualization, writing—review and editing, supervision. B.Y. Li: methodology, writing—original draft, investigation. W.B. Geng: methodology, writing—original draft, investigation. W. Yin: methodology, writing—original draft, investigation. Y. Yan: writing—review and editing. H.J. Zhang: investigation. D.W. Zhang: writing—review and editing.

Competing interests

The authors declare no competing interests.

Additional information